SIAM J. SCI. COMPUT.
Vol. 35, No. 1, pp. B248–B274

MODELING BACKWARD WAVE PROPAGATION IN METAMATERIALS BY THE FINITE ELEMENT TIME-DOMAIN METHOD*

YUNQING HUANG†, JICHUN LI‡, AND WEI YANG†

Abstract. In this paper we develop a leap-frog-type finite element method for modeling the electromagnetic wave propagation in metamaterials. The metamaterial model equations are represented by integrodifferential Maxwell's equations, which are quite challenging to analyze and solve in that we have to solve a coupled problem with different partial differential equations given in different material regions. Our method is based on a mixed finite element method using edge elements, which can easily handle the tangential continuity of the electric field. Stability analysis and optimal error estimate are carried out for the proposed scheme. The scheme is implemented and confirmed to obey the proved optimal convergence rate by using a smooth analytical solution. Then the scheme is extended to model wave propagation in heterogeneous media composed of metamaterials and free space, and extensive numerical results (using a rectangular edge element, a triangular edge element, and mixed edge elements) demonstrate the effectiveness of our algorithm for modeling the exotic backward wave propagation phenomenon in metamaterials. To the best of our knowledge, this is the first paper with an exhaustive simulation of backward wave propagation in metamaterials using time-domain finite element methods.

Key words. Maxwell's equations, metamaterials, backward wave propagation, finite element method, edge elements

AMS subject classifications. 65N30, 35L15, 78-08

DOI. 10.1137/120869869

1. Introduction.

Metamaterials are artificial materials engineered to have exotic properties that may not be found in natural materials. In recent years, the most studied electromagnetic metamaterials are the so-called negative index metamaterials whose permittivity and permeability are both negative; these properties lead to negative refraction index over some frequency range. Such metamaterials are a manifestation of materials first proposed by the Russian theorist Victor Veselago in 1967 [40]. Due to various reasons, the first metamaterial with negative refractive index was not successfully constructed until 2000 by Smith et al. [36]. The unit cell of their construction is formed by split-ring resonators and conducting straight wires, and their metamaterial only works in the microwave regime. In 2001, Shelby, Smith, and Schultz [35] carried out the first experimental demonstration of the negative refractive index of metamaterials. Since 2000, many interesting constructions of metamaterials have been achieved. Details on the short history and important references of metamaterials can be found in recently published monographs (e.g., [13, 27, 11]). Potential applications of metamaterials are diverse and include remote aerospace applications (e.g., lightweight antenna), optical nanolithography, nanotechnology circuitry, near

*Submitted to the journal's Computational Methods in Science and Engineering section March 13, 2012; accepted for publication (in revised form) October 29, 2012; published electronically February 12, 2013. This work was supported by NSFC Key Project 11031006, NSFC project 11271310, MOST 2010DFR00700, National Science Foundation grant DMS-0810896, and Hunan Provincial Innovation Foundation for Postgraduate (CX201243).

http://www.siam.org/journals/sisc/35-1/86986.html

†Hunan Key Laboratory for Computation and Simulation in Science and Engineering, Xiangtan University, China (huangyq@xtu.edu.cn, yangweixtu@126.com).

‡Department of Mathematical Sciences, University of Nevada–Las Vegas, Las Vegas, NV 89154-4020 (jichun@unlv.nevada.edu).

field superlens, lenses for high-gain antennas, cloaking devices, and even methods for shielding structures from earthquakes.

Numerical simulations of metamaterials play a very important role in seeking new designs and applications of metamaterials, but most simulations to date were carried out using either the classic finite-difference time-domain (FDTD) method [38, 16], or commercial packages such as HFSS and COMSOL [41, p. 12]. Though the FDTD method is widely used in the engineering community, it has a big disadvantage when dealing with complex geometric domains [45], which is the so-called staircase effect [38].

On the other hand, though there exist many excellent works on finite element methods for solving Maxwell's equations in free space (e.g., [8, 10, 12, 18, 19, 28, 30, 31, 46] and references cited therein) and in dispersive media (cf. [3, 26, 32, 34, 42]), there are not many devoted to the development and analysis of finite element methods for Maxwell equations when metamaterials are involved. In recent years, some investigations of well-posedness and finite element analysis for time-harmonic Maxwell's equations involving metamaterials have been conducted [6, 14]. During the same time, the authors made some initial effort in developing and analyzing some finite element methods for solving the time-domain Maxwell equations when metamaterials are involved [25, 24, 22]. But our previous papers were mainly focused on the basic numerical analysis of those schemes developed for metamaterials covering the whole physical domain. In this paper, we extend our recently developed leap-frog approach [22, 24] for pure metamaterials to modeling wave propagation in heterogeneous media involving both metamaterials and free space. In order to make our scheme more efficient, we develop a leap-frog-type scheme to solve the metamaterial Maxwell equations written as a system of integrodifferential equations in two unknowns only. Compared to our previous work [22, 24] by solving four unknowns directly, the current approach will save a lot of memory space and make our algorithm more suitable for large scale simulation.

Finally, we like to remark that the stability analysis and error estimate for the mixed finite element method are more challenging than the standard Maxwell equations in free space. A totally new issue, which comes with such leap-frog schemes, is that the time step size depends on a constant C_{inv} in the inverse inequality (see (4.1) below). An accurate estimate of C_{inv} is quite challenging and was left unsolved in our previous work [24]. In this paper, we present an elegant estimate of C_{inv} for the lowest order rectangular edge element, which is widely used in practical simulation. An exact estimate of C_{inv} for general edge elements is still unavailable, since it depends on the element geometry and the order of the basis function.

Below, let us introduce some common notation [28]:

$$H(\mathrm{curl};\Omega) = \{\boldsymbol{v} \in (L^2(\Omega))^3; \quad \nabla \times \boldsymbol{v} \in (L^2(\Omega))^3\},$$

$$H_0(\mathrm{curl};\Omega) = \{\boldsymbol{v} \in H(\mathrm{curl};\Omega); \quad \boldsymbol{n} \times \boldsymbol{v} = 0 \ \text{ on } \ \partial\Omega\},$$

$$H(\mathrm{div};\Omega) = \{\boldsymbol{v} \in (L^2(\Omega))^3; \quad \nabla \cdot \boldsymbol{v} \in L^2(\Omega)\}$$

for any bounded Lipschitz polyhedral domain Ω in $\mathcal{R}^3$ with connected boundary $\partial\Omega$. Moreover, we let $(H^\alpha(\Omega))^3$ be the standard Sobolev space equipped with norm $||\cdot||_\alpha$. When $\alpha = 0$, we just denote $||\cdot||_0$ for the $(L^2(\Omega))^3$ norm. For a time-dependent function $\boldsymbol{u}(\boldsymbol{x}, t)$, we define the space $L^\infty(0, T; (H^\alpha(\Omega))^3)$ with equipped norm

$$||\boldsymbol{u}||_{L^\infty(0,T;(H^\alpha(\Omega))^3)} = \max_{0\le t\le T} ||\boldsymbol{u}(\cdot, t)||_{(H^\alpha(\Omega))^3}.$$

The rest of the paper is organized as follows. In section 2, we describe the governing equations for modeling the wave propagation in metamaterials. In section 3, we present a leap-frog finite element method for solving the time-domain Maxwell equations when metamaterials are involved. Then in section 4 we carry out the conditional stability analysis and prove the optimal error estimate for the proposed scheme. In section 5, we first present an example confirming our theoretical error analysis. Then we present four more examples demonstrating the effectiveness of our algorithm for modeling the exotic backward wave propagation phenomenon in metamaterials. Here different perfectly matched layers are analyzed and tested in our simulations using different types of mesh. Finally, we conclude the paper in section 6.

2. The governing equations. The governing equations for modeling wave propagation in negative refraction index metamaterials described by the so-called Drude model are (see a derivation in [25])

$$\epsilon_0 \frac{\partial \boldsymbol{E}}{\partial t} = \nabla \times \boldsymbol{H} - \widetilde{\boldsymbol{J}} + \boldsymbol{f} \quad \text{in } \Omega \times (0,T), \tag{2.1}$$

$$\mu_0 \frac{\partial \boldsymbol{H}}{\partial t} = -\nabla \times \boldsymbol{E} - \widetilde{\boldsymbol{K}} \quad \text{in } \Omega \times (0,T), \tag{2.2}$$

$$\frac{\partial \widetilde{\boldsymbol{J}}}{\partial t} + \Gamma_e \widetilde{\boldsymbol{J}} = \epsilon_0 \omega_{pe}^2 \boldsymbol{E} \quad \text{in } \Omega \times (0,T), \tag{2.3}$$

$$\frac{\partial \widetilde{\boldsymbol{K}}}{\partial t} + \Gamma_m \widetilde{\boldsymbol{K}} = \mu_0 \omega_{pm}^2 \boldsymbol{H} \quad \text{in } \Omega \times (0,T), \tag{2.4}$$

where $\boldsymbol{f}$ is an added source term, ϵ_0 and μ_0 are the permittivity and permeability in vacuum, respectively, ω_{pe} and ω_{pm} are the electric and magnetic plasma frequencies, respectively, Γ_e and Γ_m are the electric and magnetic damping frequencies, respectively, $\boldsymbol{E}(\boldsymbol{x},t)$ and $\boldsymbol{H}(\boldsymbol{x},t)$ are the electric and magnetic fields, respectively, and $\widetilde{\boldsymbol{J}}(\boldsymbol{x},t)$ and $\widetilde{\boldsymbol{K}}(\boldsymbol{x},t)$ are the induced electric and magnetic currents, respectively. For simplicity, we assume that the boundary of Ω is perfectly conducting so that

$$\boldsymbol{n} \times \boldsymbol{E} = \boldsymbol{0} \qquad \text{on} \quad \partial\Omega, \tag{2.5}$$

where $\boldsymbol{n}$ is the unit outward normal to $\partial\Omega$. The initial conditions for the system (2.1)–(2.4) are assumed to be

$$\begin{aligned} &\boldsymbol{E}(\boldsymbol{x},0) = \boldsymbol{E}_0(\boldsymbol{x}), \qquad \boldsymbol{H}(\boldsymbol{x},0) = \boldsymbol{H}_0(\boldsymbol{x}),\\ &\widetilde{\boldsymbol{J}}(\boldsymbol{x},0) = \widetilde{\boldsymbol{J}}_0(\boldsymbol{x}), \qquad \widetilde{\boldsymbol{K}}(\boldsymbol{x},0) = \widetilde{\boldsymbol{K}}_0(\boldsymbol{x}), \end{aligned}$$

where $\boldsymbol{E}_0, \boldsymbol{H}_0, \widetilde{\boldsymbol{J}}_0$, and $\widetilde{\boldsymbol{K}}_0$ are some given functions.

Solving (2.3), we obtain

$$\widetilde{\boldsymbol{J}}(\boldsymbol{x},t) = \widetilde{\boldsymbol{J}}_0 e^{-\Gamma_e t} + \epsilon_0 \omega_{pe}^2 \int_0^t \boldsymbol{E}(\boldsymbol{x},s) e^{-\Gamma_e (t-s)} ds \equiv \widetilde{\boldsymbol{J}}_0 e^{-\Gamma_e t} + \boldsymbol{J}(\boldsymbol{E}). \tag{2.6}$$

Similarly, solving (2.4), we have

$$\widetilde{\boldsymbol{K}} = \widetilde{\boldsymbol{K}}_0 e^{-\Gamma_m t} + \mu_0 \omega_{pm}^2 \int_0^t \boldsymbol{H}(\boldsymbol{x},s) e^{-\Gamma_m (t-s)} ds \equiv \widetilde{\boldsymbol{K}}_0 e^{-\Gamma_m t} + \boldsymbol{K}(\boldsymbol{H}). \tag{2.7}$$

Using (2.6) and (2.7), we can reduce the original system (2.1)–(2.4) to the following:

$$\epsilon_0 \frac{\partial \boldsymbol{E}}{\partial t} = \nabla \times \boldsymbol{H} + \boldsymbol{f} - \widetilde{\boldsymbol{J}}_0 e^{-\Gamma_e t} - \boldsymbol{J}(\boldsymbol{E}), \tag{2.8}$$

$$\mu_0 \frac{\partial \boldsymbol{H}}{\partial t} = -\nabla \times \boldsymbol{E} - \widetilde{\boldsymbol{K}}_0 e^{-\Gamma_m t} - \boldsymbol{K}(\boldsymbol{H}). \tag{2.9}$$

Multiplying (2.8) by a function $\boldsymbol{\phi} \in H_0(\mathrm{curl};\Omega)$ and integrating by parts, then multiplying (2.9) by a function $\boldsymbol{\psi} \in H(\mathrm{div};\Omega)$, we obtain a weak formulation of (2.8)–(2.9): find a solution $(\boldsymbol{E},\boldsymbol{H}) \in H_0(\mathrm{curl};\Omega) \times H(\mathrm{div};\Omega)$ such that

$$\epsilon_0(\boldsymbol{E}_t,\boldsymbol{\phi}) - (\boldsymbol{H},\nabla\times\boldsymbol{\phi}) + (\boldsymbol{J}(\boldsymbol{E}),\boldsymbol{\phi}) = -(\widetilde{\boldsymbol{J}}_0 e^{-\Gamma_e t},\boldsymbol{\phi}) + (\boldsymbol{f},\boldsymbol{\phi}), \tag{2.10}$$

$$\mu_0(\boldsymbol{H}_t,\boldsymbol{\psi}) + (\nabla\times\boldsymbol{E},\boldsymbol{\psi}) + (\boldsymbol{K}(\boldsymbol{H}),\boldsymbol{\psi}) = -(\widetilde{\boldsymbol{K}}_0 e^{-\Gamma_m t},\boldsymbol{\psi}) \tag{2.11}$$

hold true for any $(\boldsymbol{\phi},\boldsymbol{\psi}) \in H_0(\mathrm{curl};\Omega) \times H(\mathrm{div};\Omega)$.

3. Design of the algorithm. To design a finite element method to solve (2.10)–(2.11), we partition Ω by a family of regular cubic (or tetrahedral) meshes T^h with maximum mesh size h. To accommodate the $H(\mathrm{curl};\Omega)$ conformity, we employ the so-called Raviart–Thomas–Nédélec mixed finite element spaces (cf. [28, 29]): on a tetrahedral mesh T^h,

$$\boldsymbol{U}_h = \{\boldsymbol{u}_h \in H(\mathrm{div};\Omega):\ \boldsymbol{u}_h|_K \in (p_{k-1})^3 \oplus \tilde{p}_{k-1}\boldsymbol{x}\ \ \forall\, K \in T^h\},$$
$$\boldsymbol{V}_h = \{\boldsymbol{v}_h \in H(\mathrm{curl};\Omega):\ \boldsymbol{v}_h|_K \in (p_{k-1})^3 \oplus S_k\ \ \forall\, K \in T^h\},$$

where $S_k = \{\vec{p} \in (\tilde{p}_k)^3, \boldsymbol{x}\cdot\vec{p} = 0\}$, and $\tilde{p}_k$ denotes the space of homogeneous polynomials of degree k, while on a cubic mesh T^h,

$$\boldsymbol{U}_h = \{\boldsymbol{u}_h \in H(\mathrm{div};\Omega):\ \boldsymbol{u}_h|_K \in Q_{k,k-1,k-1} \times Q_{k-1,k,k-1} \times Q_{k-1,k-1,k}\ \ \forall\, K \in T^h\},$$
$$\boldsymbol{V}_h = \{\boldsymbol{v}_h \in H(\mathrm{curl};\Omega):\ \boldsymbol{v}_h|_K \in Q_{k-1,k,k} \times Q_{k,k-1,k} \times Q_{k,k,k-1}\ \ \forall\, K \in T^h\}.$$

Here $Q_{i,j,k}$ denotes the space of polynomials whose degrees are less than or equal to i,j,k in variables x,y,z, respectively.

To impose the boundary condition (2.5), we introduce the subspace

$$\boldsymbol{V}_h^0 = \{\boldsymbol{v}_h \in \boldsymbol{V}_h:\ \ \boldsymbol{n}\times\boldsymbol{v}_h = \boldsymbol{0}\}. \tag{3.1}$$

To define a fully discrete scheme, we divide the time interval $(0,T)$ into N uniform subintervals by points $0 = t_0 < t_1 < \cdots < t_N = T$, where $t_k = k\tau$. Now we can formulate a leap-frog scheme for solving (2.10)–(2.11): given proper initial approximations $\boldsymbol{E}_h^0, \boldsymbol{J}_h^0 \in \boldsymbol{V}_h^0$ and $\boldsymbol{H}_h^{\frac{1}{2}}, \boldsymbol{K}_h^{\frac{1}{2}} \in \boldsymbol{U}_h$, for any $k \ge 0$ find $\boldsymbol{E}_h^k \in \boldsymbol{V}_h^0$ and $\boldsymbol{H}_h^{k+\frac{1}{2}} \in \boldsymbol{U}_h$ such that

$$\epsilon_0\left(\frac{\boldsymbol{E}_h^{k+1}-\boldsymbol{E}_h^k}{\tau},\boldsymbol{\phi}_h\right) - (\boldsymbol{H}_h^{k+\frac{1}{2}},\nabla\times\boldsymbol{\phi}_h) + \left(\frac{1}{2}(\boldsymbol{J}_h^{k+1}+\boldsymbol{J}_h^k),\boldsymbol{\phi}_h\right)$$
$$= -(\widetilde{\boldsymbol{J}}_0 e^{-\Gamma_e t_{k+\frac{1}{2}}},\boldsymbol{\phi}_h) + (\boldsymbol{f}^{k+\frac{1}{2}},\boldsymbol{\phi}_h), \tag{3.2}$$

$$\mu_0\left(\frac{\boldsymbol{H}_h^{k+\frac{3}{2}}-\boldsymbol{H}_h^{k+\frac{1}{2}}}{\tau},\boldsymbol{\psi}_h\right) + (\nabla\times\boldsymbol{E}_h^{k+1},\boldsymbol{\psi}_h) + \left(\frac{1}{2}(\boldsymbol{K}_h^{k+\frac{3}{2}}+\boldsymbol{K}_h^{k+\frac{1}{2}}),\boldsymbol{\psi}_h\right)$$
$$= -(\widetilde{\boldsymbol{K}}_0 e^{-\Gamma_m t_{k+1}},\boldsymbol{\psi}_h) \tag{3.3}$$

hold true for any $\boldsymbol{\phi}_h \in \boldsymbol{V}_h^0$ and $\boldsymbol{\psi}_h \in \boldsymbol{U}_h$. Here $\boldsymbol{J}_h^k$ is a second-order approximation of $\boldsymbol{J}(\boldsymbol{E}(\boldsymbol{x}, t_k))$, and $\boldsymbol{K}_h^{k+\frac{1}{2}}$ is a second-order approximation of $\boldsymbol{K}(\boldsymbol{H}(\boldsymbol{x}, t_{k+\frac{1}{2}}))$. More specifically, we have

$$\begin{aligned}\boldsymbol{J}_h^k &\approx \epsilon_0\omega_{pe}^2 \int_0^{t_k} \boldsymbol{E}(s)e^{-\Gamma_e(t_k-s)}ds \\ &= \epsilon_0\omega_{pe}^2 \left(\int_0^{t_{k-1}} + \int_{t_{k-1}}^{t_k}\right) \boldsymbol{E}(s)e^{-\Gamma_e(t_k-s)}ds \\ &\approx e^{-\Gamma_e\tau}\boldsymbol{J}_h^{k-1} + \frac{\tau}{2}\epsilon_0\omega_{pe}^2(\boldsymbol{E}_h^k + e^{-\Gamma_e\tau}\boldsymbol{E}_h^{k-1}).\end{aligned}$$

Hence, we have the following recursive formula for updating $\boldsymbol{J}_h^k$:

$$\boldsymbol{J}_h^0 = 0,\ \boldsymbol{J}_h^k = e^{-\Gamma_e\tau}\boldsymbol{J}_h^{k-1} + \frac{\tau}{2}\epsilon_0\omega_{pe}^2(\boldsymbol{E}_h^k + e^{-\Gamma_e\tau}\boldsymbol{E}_h^{k-1})\ \ \forall\ k \geq 1. \tag{3.4}$$

Similarly, we can have a recursive formula for updating $\boldsymbol{K}_h^{k+\frac{1}{2}}$:

$$\boldsymbol{K}_h^{k+\frac{1}{2}} = e^{-\Gamma_m\tau}\boldsymbol{K}_h^{k-\frac{1}{2}} + \frac{\tau}{2}\mu_0\omega_{pm}^2(\boldsymbol{H}_h^{k+\frac{1}{2}} + e^{-\Gamma_m\tau}\boldsymbol{H}_h^{k-\frac{1}{2}})\ \ \forall\ k \geq 1. \tag{3.5}$$

From (3.4) and (3.5), we obtain

$$\begin{aligned}\frac{1}{2}(\boldsymbol{J}_h^{k+1} + \boldsymbol{J}_h^k) &= \frac{1}{2}(1 + e^{-\Gamma_e\tau})\boldsymbol{J}_h^k + \frac{\tau}{4}\epsilon_0\omega_{pe}^2(\boldsymbol{E}_h^{k+1} + e^{-\Gamma_e\tau}\boldsymbol{E}_h^k), \\ \frac{1}{2}(\boldsymbol{K}_h^{k+\frac{3}{2}} + \boldsymbol{K}_h^{k+\frac{1}{2}}) &= \frac{1}{2}(1 + e^{-\Gamma_m\tau})\boldsymbol{K}_h^k + \frac{\tau}{4}\mu_0\omega_{pm}^2(\boldsymbol{H}_h^{k+\frac{3}{2}} + e^{-\Gamma_m\tau}\boldsymbol{H}_h^{k+\frac{1}{2}});\end{aligned}$$

substituting this into (3.2) and (3.3), we can see that the scheme (3.2)–(3.3) is equivalent to solving the following system:

$$\begin{aligned}&\frac{\epsilon_0}{\tau}\left(1 + \frac{1}{4}\omega_{pe}^2\tau^2\right)(\boldsymbol{E}_h^{k+1}, \boldsymbol{\phi}_h) = \frac{\epsilon_0}{\tau}\left(1 - \frac{1}{4}\omega_{pe}^2\tau^2\right)(\boldsymbol{E}_h^k, \boldsymbol{\phi}_h) + (\boldsymbol{H}_h^{k+\frac{1}{2}}, \nabla \times \boldsymbol{\phi}_h) \\ &\quad -\frac{1}{2}(1 + e^{-\Gamma_e\tau})(\boldsymbol{J}_h^k, \boldsymbol{\phi}_h) - e^{-\Gamma_e t_{k+\frac{1}{2}}}(\widetilde{\boldsymbol{J}}_0, \boldsymbol{\phi}_h) + (\boldsymbol{f}^{k+\frac{1}{2}}, \boldsymbol{\phi}_h),\end{aligned} \tag{3.6}$$

$$\begin{aligned}&\frac{\mu_0}{\tau}\left(1 + \frac{1}{4}\omega_{pm}^2\tau^2\right)(\boldsymbol{H}_h^{k+\frac{3}{2}}, \boldsymbol{\psi}_h) = \frac{\mu_0}{\tau}\left(1 - \frac{1}{4}\omega_{pm}^2\tau^2\right)(\boldsymbol{H}_h^{k+\frac{1}{2}}, \boldsymbol{\psi}_h) - (\nabla \times \boldsymbol{E}_h^{k+1}, \boldsymbol{\psi}_h) \\ &\quad -\frac{1}{2}(1 + e^{-\Gamma_m\tau})(\boldsymbol{K}_h^{k+\frac{1}{2}}, \boldsymbol{\psi}_h) - e^{-\Gamma_m t_{k+1}}(\widetilde{\boldsymbol{K}}_0, \boldsymbol{\psi}_h);\end{aligned} \tag{3.7}$$

i.e., at each time step, we can first solve (3.6) for $\boldsymbol{E}_h^{k+1}$, then solve (3.7) for $\boldsymbol{H}_h^{k+\frac{3}{2}}$.

4. Analysis of the numerical scheme. In this section, we carry out the stability analysis and error estimate analysis for our scheme (3.2)–(3.3).

LEMMA 4.1. *For any $k \geq 1$, we have*

$$\text{(i)}\ \ ||\boldsymbol{J}_h^k||_0 \leq \tau\epsilon_0\omega_{pe}^2 \sum_{i=0}^{k} ||\boldsymbol{E}_h^i||_0,$$

$$\text{(ii)}\ \ ||\boldsymbol{K}_h^{k+\frac{1}{2}}||_0 \leq ||\boldsymbol{K}_h^{\frac{1}{2}}||_0 + \tau\mu_0\omega_{pm}^2 \sum_{i=0}^{k} ||\boldsymbol{H}_h^{i+\frac{1}{2}}||_0.$$

Proof. (i) By the definition of $\boldsymbol{J}_h^k$, we have

$$\begin{aligned}||\boldsymbol{J}_h^k||_0 &\le ||\boldsymbol{J}_h^{k-1}||_0 + \frac{\tau}{2}\epsilon_0\omega_{pe}^2(||\boldsymbol{E}_h^{k-1}||_0 + ||\boldsymbol{E}_h^k||_0)\\ &\le ||\boldsymbol{J}_h^{k-2}||_0 + \frac{\tau}{2}\epsilon_0\omega_{pe}^2(||\boldsymbol{E}_h^{k-2}||_0 + 2||\boldsymbol{E}_h^{k-1}||_0 + ||\boldsymbol{E}_h^k||_0)\\ &\le \cdots\\ &\le ||\boldsymbol{J}_h^1||_0 + \frac{\tau}{2}\epsilon_0\omega_{pe}^2(||\boldsymbol{E}_h^1||_0 + 2||\boldsymbol{E}_h^2||_0 + \cdots + 2||\boldsymbol{E}_h^{k-1}||_0 + ||\boldsymbol{E}_h^k||_0)\\ &\le \tau\epsilon_0\omega_{pe}^2\sum_{i=0}^{k}||\boldsymbol{E}_h^i||_0,\end{aligned}$$

which completes the proof of (i). Note that we used the fact that $\boldsymbol{J}_h^0 = 0$ in the last step.

(ii) Using the definition of $\boldsymbol{K}_h^{k+\frac{1}{2}}$, we have

$$\begin{aligned}||\boldsymbol{K}_h^{k+\frac{1}{2}}||_0 &\le ||\boldsymbol{K}_h^{k-\frac{1}{2}}||_0 + \frac{\tau}{2}\mu_0\omega_{pm}^2(||\boldsymbol{H}_h^{k-\frac{1}{2}}||_0 + ||\boldsymbol{H}_h^{k+\frac{1}{2}}||_0)\\ &\le ||\boldsymbol{K}_h^{k-\frac{3}{2}}||_0 + \frac{\tau}{2}\mu_0\omega_{pm}^2(||\boldsymbol{H}_h^{k-\frac{3}{2}}||_0 + 2||\boldsymbol{H}_h^{k-\frac{1}{2}}||_0 + ||\boldsymbol{H}_h^{k+\frac{1}{2}}||_0)\\ &\le \cdots\\ &\le ||\boldsymbol{K}_h^{\frac{1}{2}}||_0 + \frac{\tau}{2}\mu_0\omega_{pm}^2(||\boldsymbol{H}_h^{\frac{1}{2}}||_0 + 2||\boldsymbol{H}_h^{\frac{3}{2}}||_0 + \cdots + 2||\boldsymbol{H}_h^{k-\frac{1}{2}}||_0 + ||\boldsymbol{H}_h^{k+\frac{1}{2}}||_0),\end{aligned}$$

which concludes the proof. ∎

Denote $C_v = \frac{1}{\sqrt{\epsilon_0\mu_0}}$ for the wave propagation speed in free space, and $C_{inv} > 0$ for the constant in the standard inverse inequality:

$$||\nabla\times\boldsymbol{\phi}_h||_0 \le C_{inv}h^{-1}||\boldsymbol{\phi}_h||_0 \quad \forall\ \boldsymbol{\phi}_h \in \boldsymbol{V}_h^0. \tag{4.1}$$

THEOREM 4.2. *If the time step τ satisfies the CFL condition*

$$\tau \le \min\left(1, \frac{1}{C_{inv}C_v}h\right), \tag{4.2}$$

then for any $n \ge 1$ we have

$$\begin{aligned}&\epsilon_0||\boldsymbol{E}_h^n||_0^2 + \mu_0||\nabla\times\boldsymbol{H}_h^{n+\frac{1}{2}}||_0^2\\ &\le C(||\boldsymbol{H}_h^{\frac{1}{2}}||_0^2 + ||\nabla\times\boldsymbol{E}_h^0||_0^2 + ||\widetilde{\boldsymbol{J}}_0||_0^2 + ||\widetilde{\boldsymbol{K}}_0||_0^2 + ||\boldsymbol{K}_h^{\frac{1}{2}}||_0^2 + ||\boldsymbol{f}||_{L^\infty(0,T;L^2(\Omega)^3)}^2),\end{aligned}$$

where the positive constant C depends on physical parameters $\Gamma_e, \Gamma_m, \omega_{pe}, \omega_{pm}, T, \epsilon_0$, and μ_0.

Proof. Choosing $\boldsymbol{\phi}_h = \frac{\tau}{2}(\boldsymbol{E}_h^{k+1} + \boldsymbol{E}_h^k) = \tau\overline{\boldsymbol{E}}_h^{k+\frac{1}{2}}$ and $\boldsymbol{\psi}_h = \frac{\tau}{2}(\boldsymbol{H}_h^{k+\frac{3}{2}} + \boldsymbol{H}_h^{k+\frac{1}{2}}) = \tau\overline{\boldsymbol{H}}_h^{k+1}$ in (3.2) and (3.3), respectively, and adding the resultants together, we obtain

$$\begin{aligned}&\frac{\epsilon_0}{2}(||\boldsymbol{E}_h^{k+1}||_0^2 - ||\boldsymbol{E}_h^k||_0^2) + \frac{\mu_0}{2}(||\boldsymbol{H}_h^{k+\frac{3}{2}}||_0^2 - ||\boldsymbol{H}_h^{k+\frac{1}{2}}||_0^2)\\ &+\frac{\tau^2}{4}\epsilon_0\omega_{pe}^2(\boldsymbol{E}_h^{k+1} + e^{-\Gamma_e\tau}\boldsymbol{E}_h^k, \overline{\boldsymbol{E}}_h^{k+\frac{1}{2}}) + \frac{\tau^2}{4}\mu_0\omega_{pm}^2(\boldsymbol{H}_h^{k+\frac{3}{2}} + e^{-\Gamma_m\tau}\boldsymbol{H}_h^{k+\frac{1}{2}}, \overline{\boldsymbol{H}}_h^{k+1})\\ &= \frac{\tau}{2}\left[(\boldsymbol{H}_h^{k+\frac{1}{2}}, \nabla\times\overline{\boldsymbol{E}}_h^{k+\frac{1}{2}}) - (\nabla\times\boldsymbol{E}_h^{k+1}, \overline{\boldsymbol{H}}_h^{k+1})\right]\\ &- \tau\left(\frac{1}{2}(1+e^{-\Gamma_e\tau})\boldsymbol{J}_h^k, \overline{\boldsymbol{E}}_h^{k+\frac{1}{2}}\right) + \tau(\boldsymbol{f}^{k+\frac{1}{2}}, \overline{\boldsymbol{E}}_h^{k+\frac{1}{2}})\\ &- \tau\left(\frac{1}{2}(1+e^{-\Gamma_m\tau})\boldsymbol{K}_h^{k+\frac{1}{2}}, \overline{\boldsymbol{H}}_h^{k+1}\right) - \tau e^{-\Gamma_e t_{k+\frac{1}{2}}}(\widetilde{\boldsymbol{J}}_0, \overline{\boldsymbol{E}}_h^{k+\frac{1}{2}}) - \tau e^{-\Gamma_m t_{k+1}}(\widetilde{\boldsymbol{K}}_0, \overline{\boldsymbol{H}}_h^{k+1}).\end{aligned} \tag{4.3}$$

Using the inequality $(\sum_{i=0}^{k} a_i)^2 \le (\sum_{i=0}^{k} 1^2)(\sum_{i=0}^{k} a_i^2)$ and Lemma 4.1, we have

$$||\boldsymbol{J}_h^k||_0^2 \le \tau^2(\epsilon_0\omega_{pe}^2)^2(k+1)\sum_{i=0}^{k}||\boldsymbol{E}_h^i||_0^2 \le CT\tau\sum_{i=0}^{k}||\boldsymbol{E}_h^i||_0^2.$$

From this and the standard arithmetic-geometric mean inequality we obtain

$$\tau\left(\frac{1}{2}(1+e^{-\Gamma_e\tau})\boldsymbol{J}_h^k, \overline{\boldsymbol{E}}_h^{k+\frac{1}{2}}\right) \le 2\tau\delta_1||\overline{\boldsymbol{E}}_h^{k+\frac{1}{2}}||_0^2 + \frac{\tau}{8\delta_1}||\frac{1}{2}(1+e^{-\Gamma_e\tau})\boldsymbol{J}_h^k||_0^2$$
$$\le \tau\delta_1(||\boldsymbol{E}_h^{k+1}||_0^2 + ||\boldsymbol{E}_h^k||_0^2) + \frac{CT\tau^2}{\delta_1}\sum_{i=0}^{k}||\boldsymbol{E}_h^i||_0^2.$$

Similarly, by Lemma 4.1, we have

$$||\boldsymbol{K}_h^{k+\frac{1}{2}}||_0^2 \le 2\left[||\boldsymbol{K}_h^{\frac{1}{2}}||_0^2 + (\tau\mu_0\omega_{pm}^2)^2\left(\sum_{i=0}^{k}||\boldsymbol{H}_h^{i+\frac{1}{2}}||_0\right)^2\right]$$
$$\le 2||\boldsymbol{K}_h^{\frac{1}{2}}||_0^2 + 2\tau^2(\mu_0\omega_{pm}^2)^2(k+1)\sum_{i=0}^{k}||\boldsymbol{H}_h^{i+\frac{1}{2}}||_0^2$$
$$\le 2||\boldsymbol{K}_h^{\frac{1}{2}}||_0^2 + 2T\tau(\mu_0\omega_{pm}^2)^2\sum_{i=0}^{k}||\boldsymbol{H}_h^{i+\frac{1}{2}}||_0^2.$$

From this and the arithmetic-geometric mean inequality we obtain

$$\tau\left(\frac{1}{2}(1+e^{-\Gamma_m\tau})\boldsymbol{K}_h^{k+\frac{1}{2}}, \overline{\boldsymbol{H}}_h^{k+1}\right)$$
$$\le \tau\delta_2(||\boldsymbol{H}_h^{k+\frac{3}{2}}||_0^2 + ||\boldsymbol{H}_h^{k+\frac{1}{2}}||_0^2) + \frac{CT\tau^2}{\delta_2}\sum_{i=0}^{k}||\boldsymbol{H}_h^{i+\frac{1}{2}}||_0^2 + \frac{\tau}{4\delta_2}||\boldsymbol{K}_h^{\frac{1}{2}}||_0^2.$$

By the Cauchy–Schwarz inequality, we have

$$\tau e^{-\Gamma_e t_{k+\frac{1}{2}}}(\widetilde{\boldsymbol{J}}_0, \overline{\boldsymbol{E}}_h^{k+\frac{1}{2}}) \le \tau\delta_3(||\boldsymbol{E}_h^{k+1}||_0^2 + ||\boldsymbol{E}_h^k||_0^2) + \frac{\tau}{8\delta_3}||\widetilde{\boldsymbol{J}}_0||_0^2,$$
$$\tau(\boldsymbol{f}^{k+\frac{1}{2}}, \overline{\boldsymbol{E}}_h^{k+\frac{1}{2}}) \le \tau\delta_4(||\boldsymbol{E}_h^{k+1}||_0^2 + ||\boldsymbol{E}_h^k||_0^2) + \frac{\tau}{8\delta_4}||\boldsymbol{f}^{k+\frac{1}{2}}||_0^2,$$

and

$$\tau e^{-\Gamma_m t_{k+1}}(\widetilde{\boldsymbol{K}}_0, \overline{\boldsymbol{K}}_h^{k+1}) \le \tau\delta_5(||\boldsymbol{H}_h^{k+\frac{3}{2}}||_0^2 + ||\boldsymbol{H}_h^{k+\frac{1}{2}}||_0^2) + \frac{\tau}{8\delta_5}||\widetilde{\boldsymbol{K}}_0||_0^2.$$

Furthermore, by the Cauchy–Schwarz inequality, we have

$$(\boldsymbol{E}_h^{k+1} + e^{-\Gamma_e\tau}\boldsymbol{E}_h^k, \overline{\boldsymbol{E}}_h^{k+\frac{1}{2}}) = \frac{1}{2}[||\boldsymbol{E}_h^{k+1}||_0^2 + e^{-\Gamma_e\tau}||\boldsymbol{E}_h^k||_0^2 + (1+e^{-\Gamma_e\tau})(\boldsymbol{E}_h^{k+1}, \boldsymbol{E}_h^k)]$$
$$\ge \frac{1}{4}(1-e^{-\Gamma_e\tau})(||\boldsymbol{E}_h^{k+1}||_0^2 - ||\boldsymbol{E}_h^k||_0^2).$$

By the same argument, we can obtain

$$(\boldsymbol{H}_h^{k+\frac{3}{2}} + e^{-\Gamma_m\tau}\boldsymbol{H}_h^{k+\frac{1}{2}}, \overline{\boldsymbol{H}}_h^{k+1}) \ge \frac{1}{4}(1-e^{-\Gamma_m\tau})(||\boldsymbol{H}_h^{k+\frac{3}{2}}||_0^2 - ||\boldsymbol{H}_h^{k+\frac{1}{2}}||_0^2).$$

Substituting the above estimates into (4.3), using the identity

$$\begin{aligned}&(\boldsymbol{H}_h^{k+\frac{1}{2}}, \nabla\times(\boldsymbol{E}_h^{k+1}+\boldsymbol{E}_h^k)) - (\nabla\times\boldsymbol{E}_h^{k+1}, \boldsymbol{H}_h^{k+\frac{3}{2}}+\boldsymbol{H}_h^{k+\frac{1}{2}})\\ &= (\boldsymbol{H}_h^{k+\frac{1}{2}}, \nabla\times\boldsymbol{E}_h^k) - (\boldsymbol{H}_h^{k+\frac{3}{2}}, \nabla\times\boldsymbol{E}_h^{k+1}),\end{aligned}$$

and summing up the resultant from $k=1$ to $n-1$, we have

$$\begin{aligned}&\frac{\epsilon_0}{2}\left(1+\tau^2\omega_{pe}^2\frac{1-e^{-\Gamma_e\tau}}{8}\right)(||\boldsymbol{E}_h^n||_0^2 - ||\boldsymbol{E}_h^k||_0^2)\\ &+\frac{\mu_0}{2}\left(1+\tau^2\omega_{pm}^2\frac{1-e^{-\Gamma_m\tau}}{8}\right)(||\boldsymbol{H}_h^{n+\frac{1}{2}}||_0^2 - ||\boldsymbol{H}_h^{\frac{1}{2}}||_0^2)\\ &\le \frac{\tau}{2}[(\boldsymbol{H}_h^{\frac{1}{2}}, \nabla\times\boldsymbol{E}_h^0) - (\boldsymbol{H}_h^{n+\frac{1}{2}}, \nabla\times\boldsymbol{E}_h^n)] + \tau(\delta_1+\delta_3+\delta_4)\left(||\boldsymbol{E}_h^n||_0^2 + 2\sum_{k=0}^{n-1}||\boldsymbol{E}_h^k||_0^2\right)\\ &+\frac{CT\tau^2}{\delta_1}n\sum_{k=0}^{n-1}||\boldsymbol{E}_h^k||_0^2 + \tau(\delta_2+\delta_5)\left(||\boldsymbol{H}_h^{n+\frac{1}{2}}||_0^2 + 2\sum_{k=0}^{n-1}||\boldsymbol{H}_h^{k+\frac{1}{2}}||_0^2\right)\\ &+\frac{CT\tau^2}{\delta_2}n\sum_{k=0}^{n-1}||\boldsymbol{H}_h^{k+\frac{1}{2}}||_0^2 + \frac{n\tau}{4\delta_2}||\boldsymbol{K}_h^{\frac{1}{2}}||_0^2 + \frac{n\tau}{8\delta_3}||\widetilde{\boldsymbol{J}}_0||_0^2 + \frac{n\tau}{8\delta_5}||\widetilde{\boldsymbol{K}}_0||_0^2 + \frac{\tau}{8\delta_4}\sum_{k=0}^{n-1}||\boldsymbol{f}^{k+\frac{1}{2}}||_0^2.\end{aligned} \tag{4.4}$$

Using the Cauchy–Schwarz inequality and the inverse inequality (4.1), we have

$$\begin{aligned}\tau(\boldsymbol{H}_h^{n+\frac{1}{2}}, \nabla\times\boldsymbol{E}_h^n) &\le \tau\cdot C_{inv}h^{-1}||\boldsymbol{H}_h^{n+\frac{1}{2}}||_0||\boldsymbol{E}_h^n||_0\\ &= \tau\cdot C_{inv}h^{-1}\cdot C_v\sqrt{\mu_0}||\boldsymbol{H}_h^{n+\frac{1}{2}}||_0\cdot\sqrt{\epsilon_0}||\boldsymbol{E}_h^n||_0\\ &\le \frac{C_{inv}C_v\tau}{2h}(\mu_0||\boldsymbol{H}_h^{n+\frac{1}{2}}||_0^2 + \epsilon_0||\boldsymbol{E}_h^n||_0^2).\end{aligned} \tag{4.5}$$

Substituting (4.5) into (4.4), choosing $\tau \le \min(1, \frac{h}{C_{inv}C_v})$ and δ_i small enough, and then using the discrete Gronwall inequality, we conclude the proof. ∎

Now let us analyze the error estimate for our scheme (3.2)–(3.3). Let $\xi_h^k = \Pi_h\boldsymbol{E}^k - \boldsymbol{E}_h^k$ and $\eta_h^k = P_h\boldsymbol{H}^k - \boldsymbol{H}_h^k$, where $\Pi_h\boldsymbol{E}\in\boldsymbol{V}_h$ denotes the standard Nédélec interpolation [28, 29], and $P_h\boldsymbol{H}$ denotes the L^2 projection onto the space $\boldsymbol{U}_h$.

Integrating (2.10) from $t=t_k$ to t_{k+1}, integrating (2.11) from $t=t_{k+\frac{1}{2}}$ to $t_{k+\frac{3}{2}}$, then subtracting the resultants divided by τ from (3.2) and (3.3), respectively, we obtain the error equations

$$\begin{aligned}&\epsilon_0\left(\frac{\xi_h^{k+1}-\xi_h^k}{\tau}, \boldsymbol{\phi}_h\right) - (\eta_h^{k+\frac{1}{2}}, \nabla\times\boldsymbol{\phi}_h) + \left(\Pi_h\left(\frac{\boldsymbol{J}^{k+1}+\boldsymbol{J}^k}{2}\right) - \frac{\boldsymbol{J}_h^{k+1}+\boldsymbol{J}_h^k}{2}, \boldsymbol{\phi}_h\right)\\ &= \epsilon_0\left(\frac{(\Pi_h\boldsymbol{E}^{k+1}-\boldsymbol{E}^{k+1}) - (\Pi_h\boldsymbol{E}^k-\boldsymbol{E}^k)}{\tau}, \boldsymbol{\phi}_h\right) - \left(P_h\boldsymbol{H}^{k+\frac{1}{2}} - \frac{1}{\tau}\int_{t_k}^{t_{k+1}}\boldsymbol{H}(s)ds, \nabla\times\boldsymbol{\phi}_h\right)\\ &+\left(\Pi_h\left(\frac{\boldsymbol{J}^{k+1}+\boldsymbol{J}^k}{2}\right) - \frac{1}{\tau}\int_{t_k}^{t_{k+1}}\boldsymbol{J}(\boldsymbol{E}(s))ds, \boldsymbol{\phi}_h\right)\\ &+\left(e^{-\Gamma_e t_{k+\frac{1}{2}}} - \frac{1}{\tau}\int_{t_k}^{t_{k+1}}e^{-\Gamma_e s}ds\right)(\widetilde{\boldsymbol{J}}_0, \boldsymbol{\phi}_h) + \left(\frac{1}{\tau}\int_{t_k}^{t_{k+1}}\boldsymbol{f}(s)ds - \boldsymbol{f}^{k+\frac{1}{2}}, \boldsymbol{\phi}_h\right)\end{aligned} \tag{4.6}$$

and

$$
\begin{aligned}
&\mu_0\left(\frac{\eta_h^{k+\frac{3}{2}}-\eta_h^{k+\frac{1}{2}}}{\tau},\boldsymbol{\psi}_h\right)+(\nabla\times\xi_h^{k+1},\boldsymbol{\psi}_h)\\
&+\left(P_h\left(\frac{\boldsymbol{K}^{k+\frac{3}{2}}+\boldsymbol{K}^{k+\frac{1}{2}}}{2}\right)-\frac{\boldsymbol{K}_h^{k+\frac{3}{2}}+\boldsymbol{K}_h^{k+\frac{1}{2}}}{2},\boldsymbol{\psi}_h\right)\\
&=\mu_0\left(\frac{(P_h\boldsymbol{H}^{k+\frac{3}{2}}-\boldsymbol{H}^{k+\frac{3}{2}})-(P_h\boldsymbol{H}^{k+\frac{1}{2}}-\boldsymbol{H}^{k+\frac{1}{2}})}{\tau},\boldsymbol{\psi}_h\right)\\
&+\left(\nabla\times\left(\Pi_h\boldsymbol{E}^{k+1}-\frac{1}{\tau}\int_{t_{k+\frac{1}{2}}}^{t_{k+\frac{3}{2}}}\boldsymbol{E}(s)ds\right),\boldsymbol{\psi}_h\right)\\
&+\left(P_h\left(\frac{\boldsymbol{K}^{k+\frac{3}{2}}+\boldsymbol{K}^{k+\frac{1}{2}}}{2}\right)-\frac{1}{\tau}\int_{t_{k+\frac{1}{2}}}^{t_{k+\frac{3}{2}}}\boldsymbol{K}(\boldsymbol{H}(s))ds,\boldsymbol{\psi}_h\right)\\
&+\left(e^{-\Gamma_m t_{k+1}}-\frac{1}{\tau}\int_{t_{k+\frac{1}{2}}}^{t_{k+\frac{3}{2}}}e^{-\Gamma_m s}ds\right)(\widetilde{\boldsymbol{K}}_0,\boldsymbol{\psi}_h).
\end{aligned}
\tag{4.7}
$$

Using a technique similar to the one developed in the above stability analysis, and using the interpolation estimate (see [29, Theorem 2] and [28, Theorem 5.41])

$$||\boldsymbol{u}-\Pi_h\boldsymbol{u}||_0+||\nabla\times(\boldsymbol{u}-\Pi_h\boldsymbol{u})||_0\le Ch^l||\boldsymbol{u}||_{l+1}\ \ \forall\ \boldsymbol{u}\in(H^{l+1}(\Omega))^3,\frac{1}{2}<l\le k$$

and the estimate for the L^2 projection onto $\boldsymbol{U}_h$ (see [29, Theorem 4] and [28, Theorem 5.25]),

$$||\boldsymbol{u}-P_h\boldsymbol{u}||_0\le Ch^l||\boldsymbol{u}||_{l+1}\ \ \forall\ \boldsymbol{u}\in(H^{l+1}(\Omega))^3,\frac{1}{2}<l\le k,$$

we can obtain the following optimal error estimate.

THEOREM 4.3. *Assume that the initial approximations $\boldsymbol{E}_h^0$ and $\boldsymbol{H}_h^{\frac{1}{2}}$ satisfy the condition $||\boldsymbol{E}^0-\boldsymbol{E}_h^0||_0+||\boldsymbol{H}^{\frac{1}{2}}-\boldsymbol{H}_h^{\frac{1}{2}}||_0=O(\tau^2+h^k)$, and the analytical solutions $\boldsymbol{E}(\boldsymbol{x},t)$ and $\boldsymbol{H}(\boldsymbol{x},t)$ are smooth enough. Then we have*

$$\max_{n\ge1}(||\boldsymbol{E}^n-\boldsymbol{E}_h^n||_0+||\boldsymbol{H}^{n+\frac{1}{2}}-\boldsymbol{H}_h^{n+\frac{1}{2}}||_0)\le C(\tau^2+h^k)\quad\forall\ k\ge1,\tag{4.8}$$

where k is the degree of basis functions in spaces $\boldsymbol{U}_h$ and $\boldsymbol{V}_h$.

Remark 4.1. Theorem 4.3 shows that the optimal error estimate in the L^2 norm is only $O(h^k)$ for the kth order edge element $Q_{k-1,k,k}\times Q_{k,k-1,k}\times Q_{k,k,k-1}$, the reason being that the basis functions do not contain all the kth-order bases like the standard Lagrange element $Q_{k,k,k}$. The theoretical analysis is justified by our numerical result given in Example 1 of section 5, where the lowest-order rectangular edge element $Q_{0,1}\times Q_{1,0}$ is used and the observed L^2 error given in Table 1 is $O(h)$. In this case, the basis functions of $Q_{0,1}\times Q_{1,0}$ do not include all the bases $1,x,y,xy$ like the standard Lagrange element $Q_{1,1}$.

5. Numerical results. In this section, we provide some two-dimensional (2D) examples showing the effectiveness of our algorithm. We want to mention that the stability analysis and error estimates derived above hold true for both 2D and 3D

problems. In the 2D case, we just need to distinguish between the scalar and vector curl operators

$$\nabla \times \boldsymbol{E} = \frac{\partial E_y}{\partial x} - \frac{\partial E_x}{\partial y} \quad \text{for any vector } \boldsymbol{E} = (E_x, E_y)',$$
$$\nabla \times H = \left(\frac{\partial H}{\partial y}, -\frac{\partial H}{\partial x}\right)' \quad \text{for any scalar } H.$$

Without loss of generality, we consider the 2D transverse electromagnetic (TE) model, in which case we have three unknowns: the vector electric field $\boldsymbol{E} = (E_x, E_y)'$, and the scalar magnetic field $H = H_z$. In 2D, the Raviart–Thomas–Nédélec rectangular elements are represented as

$$\boldsymbol{U}_h = \{u_h \in L^2(\Omega) : \ u_h|_K \in Q_{k-1,k-1} \quad \forall\, K \in T^h\}, \quad k \geq 1, \tag{5.1}$$
$$\boldsymbol{V}_h = \{\boldsymbol{v}_h \in H(\mathrm{curl}; \Omega) : \ \boldsymbol{v}_h|_K \in Q_{k-1,k} \times Q_{k,k-1} \quad \forall\, K \in T^h\}, \quad k \geq 1. \tag{5.2}$$

In this paper, we implemented only the lowest-order basis function, i.e., $k = 1$.

Before we move on, we want to address a practical issue on the constant C_{inv} in (4.1), which affects the choice of the time step τ. An accurate estimate of C_{inv} is quite challenging, since it depends on element geometries and the orders of the basis functions. Harari and Hughes [17] explicitly obtained C_{inv} for some inverse inequalities. Schwab [33] and Warburton and Hesthaven [43] derived some explicit expressions for hp-finite element inverse inequalities. To the best of our knowledge, no work exists for the exact derivation of C_{inv} for edge elements.

5.1. Exact evaluation of C_{inv}. For simplicity, below we consider the lowest-order edge element basis functions on a general rectangle $K = [x_c - h_x, x_c + h_x] \times [y_c - h_y, y_c + h_y]$:

$$\boldsymbol{\psi}_1^h = \begin{pmatrix} \frac{(y_c+h_y)-y}{4h_xh_y} \\ 0 \end{pmatrix}, \quad \boldsymbol{\psi}_2^h = \begin{pmatrix} 0 \\ \frac{x-(x_c-h_x)}{4h_xh_y} \end{pmatrix},$$
$$\boldsymbol{\psi}_3^h = \begin{pmatrix} \frac{(y_c-h_y)-y}{4h_xh_y} \\ 0 \end{pmatrix}, \quad \boldsymbol{\psi}_4^h = \begin{pmatrix} 0 \\ \frac{x-(x_c+h_x)}{4h_xh_y} \end{pmatrix},$$

where $\boldsymbol{\psi}_j^h, j = 1, 2, 3, 4$, start from the bottom edge and are oriented counterclockwise. Hence any $\boldsymbol{v}_h \in \boldsymbol{V}_h$ with $k = 1$ in (5.2) can be expressed as $\boldsymbol{v}_h = \sum_{i=1}^4 c_i \boldsymbol{\psi}_i^h$, from which we have

$$\begin{aligned} |\nabla \times \boldsymbol{v}_h|^2_{L^2(K)} &= \int_K \left| \sum_{i=1}^4 c_i \nabla \times \boldsymbol{\psi}_i^h \right|^2 dxdy = \left(\frac{1}{4h_xh_y}\right)^2 \int_K \left| \sum_{i=1}^4 c_i \right|^2 dxdy \\ &\leq \left(\frac{1}{4h_xh_y}\right)^2 \int_K 4 \cdot \left(\sum_{i=1}^4 c_i^2\right) dxdy = \frac{1}{h_xh_y} \cdot \sum_{i=1}^4 c_i^2. \end{aligned} \tag{5.3}$$

On the other hand, by the definition of $\boldsymbol{\psi}_j^h$, we easily have

$$\begin{aligned} |\boldsymbol{v}_h|^2_{L^2(K)} &= \sum_{i=1}^4 \sum_{l=1}^4 c_i c_l \int_K \boldsymbol{\psi}_i^h \cdot \boldsymbol{\psi}_l^h dxdy \\ &= c_1^2 \int_K |\boldsymbol{\psi}_1^h|^2 + 2c_1c_3 \int_K \boldsymbol{\psi}_1^h \cdot \boldsymbol{\psi}_3^h + c_2^2 \int_K |\boldsymbol{\psi}_2^h|^2 \\ &\quad + 2c_2c_4 \int_K \boldsymbol{\psi}_2^h \cdot \boldsymbol{\psi}_4^h + c_3^2 \int_K |\boldsymbol{\psi}_3^h|^2 + c_4^2 \int_K |\boldsymbol{\psi}_4^h|^2. \end{aligned} \tag{5.4}$$

Through some lengthy calculation, it is easy to check that

$$\int_K |\boldsymbol{\psi}_1^h|^2 dxdy = \int_K |\boldsymbol{\psi}_3^h|^2 dxdy = \frac{h_y}{3h_x}, \quad \int_K |\boldsymbol{\psi}_2^h|^2 dxdy = \int_K |\boldsymbol{\psi}_4^h|^2 dxdy = \frac{h_x}{3h_y},$$

and

$$\int_K \boldsymbol{\psi}_1^h \cdot \boldsymbol{\psi}_3^h dxdy = -\frac{h_y}{6h_x}, \quad \int_K \boldsymbol{\psi}_2^h \cdot \boldsymbol{\psi}_4^h dxdy = -\frac{h_x}{6h_y};$$

substituting these into (5.4), we obtain

$$\begin{aligned} |\boldsymbol{v}_h|^2_{L^2(K)} &= \frac{h_y}{6h_x}[c_1^2 + c_3^2 + (c_1 - c_3)^2] + \frac{h_x}{6h_y}[c_2^2 + c_4^2 + (c_2 - c_4)^2] \\ &\geq \frac{h_y}{6h_x}(c_1^2 + c_3^2) + \frac{h_x}{6h_y}(c_2^2 + c_4^2) = \frac{1}{6h_xh_y}[h_y^2(c_1^2 + c_3^2) + h_x^2(c_2^2 + c_4^2)] \\ &\geq \frac{1}{6h_xh_y} h_{max}^2 \cdot \left(\frac{h_{min}}{h_{max}}\right)^2 (c_1^2 + c_2^2 + c_3^2 + c_4^2), \end{aligned} \tag{5.5}$$

where we denoted $h_{max} = \max(h_x, h_y)$ and $h_{min} = \min(h_x, h_y)$.

Combining (5.3) and (5.5), we have

$$\frac{|\nabla \times \boldsymbol{v}_h|^2_{L^2(K)}}{|\boldsymbol{v}_h|^2_{L^2(K)}} \leq 6h_{max}^{-2} \cdot \left(\frac{h_{max}}{h_{min}}\right)^2,$$

which leads to the inverse inequality (4.1) with

$$C_{inv} = \sqrt{6}\frac{h_{max}}{h_{min}}. \tag{5.6}$$

Considering the CFL constraint (4.2), in practice computation we should avoid using highly anisotropic meshes which will make the time step unreasonably small.

Remark 5.1. We like to remark that our theoretical results hold true for triangular elements. However, an exact evaluation of C_{inv} for general triangular edge elements is challenging and unavailable. Here we show the result for a mesh formed by right triangles. Note that the lowest-order triangular edge element basis functions are

$$\boldsymbol{\psi}_{ij} = \lambda_i \nabla \lambda_j - \lambda_j \nabla \lambda_i, \quad i, j = 1, 2, 3, \tag{5.7}$$

for edge P_iP_j, where λ_i denotes the linear Lagrangian basis function at the ith vertex P_i of a triangle.

Assume that the right triangle $K = P_1P_2P_3$ has vertices $P_i(x_i, y_i), i = 1, 2, 3$, the angle at P_1 is denoted as α, and the angle at P_2 is 90°. Simplifying (5.7), we obtain

$$\boldsymbol{\psi}_{12}^h = \begin{pmatrix} y_3 - y \\ x - x_3 \end{pmatrix} /2|K|, \quad \boldsymbol{\psi}_{23}^h = \begin{pmatrix} y_1 - y \\ x - x_1 \end{pmatrix} /2|K|, \quad \boldsymbol{\psi}_{31}^h = \begin{pmatrix} y_2 - y \\ x - x_2 \end{pmatrix} /2|K|,$$

where $|K|$ denotes the area of the triangle. Hence any function $\boldsymbol{v}_h \in \boldsymbol{V}_h \subset H(\text{curl}; \Omega)$ can be expressed as $\boldsymbol{v}_h = c_1\boldsymbol{\psi}_{12}^h + c_2\boldsymbol{\psi}_{23}^h + c_3\boldsymbol{\psi}_{31}^h$.

After some lengthy calculations, we have

$$\int_K |\boldsymbol{\psi}_{12}^h|^2 dxdy = \frac{1}{4|K|^2}\int_K [(y_3-y)^2+(x-x_3)^2]dxdy = \frac{1}{4}\left(\tan\alpha+\frac{1}{3}\cot\alpha\right),$$
$$\int_K |\boldsymbol{\psi}_{23}^h|^2 dxdy = \frac{1}{4|K|^2}\int_K [(y_1-y)^2+(x-x_1)^2]dxdy = \frac{1}{4}\left(\frac{1}{3}\tan\alpha+\cot\alpha\right),$$
$$\int_K |\boldsymbol{\psi}_{31}^h|^2 dxdy = \frac{1}{4|K|^2}\int_K [(y_2-y)^2+(x-x_2)^2]dxdy = \frac{1}{12}(\tan\alpha+\cot\alpha),$$
$$\int_K \boldsymbol{\psi}_{12}^h\cdot\boldsymbol{\psi}_{23}^h dxdy = -\frac{1}{12}(\tan\alpha+\cot\alpha),$$
$$\int_K \boldsymbol{\psi}_{12}^h\cdot\boldsymbol{\psi}_{31}^h dxdy = \frac{1}{12}(-\tan\alpha+\cot\alpha),$$
$$\int_K \boldsymbol{\psi}_{23}^h\cdot\boldsymbol{\psi}_{31}^h dxdy = \frac{1}{12}(\tan\alpha-\cot\alpha),$$

from which we have

$$\begin{aligned}
|\boldsymbol{v}_h|^2_{L^2(K)} &= c_1^2\int_K |\boldsymbol{\psi}_{12}^h|^2 + 2c_1c_2\int_K \boldsymbol{\psi}_{12}^h\cdot\boldsymbol{\psi}_{23}^h + 2c_1c_3\int_K \boldsymbol{\psi}_{12}^h\cdot\boldsymbol{\psi}_{31}^h \\
&\quad + c_2^2\int_K |\boldsymbol{\psi}_{23}^h|^2 + 2c_2c_3\int_K \boldsymbol{\psi}_{23}^h\cdot\boldsymbol{\psi}_{31}^h + c_3^2\int_K |\boldsymbol{\psi}_{31}^h|^2 \\
&= -\frac{2c_1c_2}{12}(\tan\alpha+\cot\alpha) - \frac{2c_1c_3}{12}(\tan\alpha-\cot\alpha) + \frac{2c_2c_3}{12}(\tan\alpha-\cot\alpha) \\
&\quad + c_1^2\left(\frac{1}{4}\tan\alpha+\frac{1}{12}\cot\alpha\right) + c_2^2\left(\frac{1}{12}\tan\alpha+\frac{1}{4}\cot\alpha\right) + c_3^2\left(\frac{1}{12}\tan\alpha+\frac{1}{12}\cot\alpha\right) \\
&= \frac{\tan\alpha+\cot\alpha}{12}(c_1-c_2)^2 + \frac{\tan\alpha-\cot\alpha}{12}(c_1-c_3)^2 + \frac{\tan\alpha-\cot\alpha}{12}(c_2-c_3)^2 \\
&\quad + \frac{\tan\alpha+\cot\alpha}{12}c_1^2 + \frac{3\cot\alpha-\tan\alpha}{12}c_2^2 + \frac{3\cot\alpha-\tan\alpha}{12}c_3^2.
\end{aligned} \tag{5.8}$$

Using the fact that $\nabla\times\boldsymbol{\psi}_{ij}^h = \frac{1}{|K|}$, we have

$$\begin{aligned}
|\nabla\times\boldsymbol{v}_h|^2_{L^2(K)} &= \int_K |c_1\nabla\times\boldsymbol{\psi}_{12}^h + c_2\nabla\times\boldsymbol{\psi}_{23}^h + c_3\nabla\times\boldsymbol{\psi}_{31}^h|^2 dxdy \\
&= \frac{1}{|K|^2}\int_K \left|\sum_{i=1}^3 c_i\right|^2 \le \frac{1}{|K|^2}\int_K 3\left(\sum_{i=1}^3 c_i^2\right) = \frac{3}{|K|}\sum_{i=1}^3 c_i^2.
\end{aligned} \tag{5.9}$$

Under the condition

$$\tan\alpha-\cot\alpha\ge 0, \quad 3\cot\alpha-\tan\alpha>0, \tag{5.10}$$

and using (5.8), (5.9) and the fact that

$$\frac{\tan\alpha+\cot\alpha}{12} = \frac{(3\cot\alpha-\tan\alpha)+2(\tan\alpha-\cot\alpha)}{12} \ge \frac{3\cot\alpha-\tan\alpha}{12},$$

we obtain

$$|\boldsymbol{v}_h|^2_{L^2(K)} \ge \frac{3\cot\alpha-\tan\alpha}{12}(c_1^2+c_2^2+c_3^2) \ge \frac{(3\cot\alpha-\tan\alpha)|K|}{36}|\nabla\times\boldsymbol{v}_h|^2_{L^2(K)}. \tag{5.11}$$

For our right triangle K, the longest edge length $h_{max} = |P_1P_3|$, from which we see that the area of the triangle $|K| = \frac{1}{2}h_{max}^2 \cos\alpha \sin\alpha$, which, applied in (5.11), gives us

$$|\nabla \times \boldsymbol{v}_h|_{L^2(K)}/|\boldsymbol{v}_h|_{L^2(K)} \le \sqrt{\frac{72}{3\cos^2\alpha - \sin^2\alpha}}h_{max}^{-1},$$

which implies that $c_{inv} = \sqrt{\frac{72}{3\cos^2\alpha - \sin^2\alpha}}$. A special case is $\alpha = 45^\circ$, which gives $c_{inv} = 6\sqrt{2}$.

Similarly, under the other condition

$$\tan\alpha - \cot\alpha \le 0, \quad 3\tan\alpha - \cot\alpha > 0, \tag{5.12}$$

and using the fact that

$$\frac{\tan\alpha + \cot\alpha}{12} = \frac{(3\tan\alpha - \cot\alpha) + 2(\cot\alpha - \tan\alpha)}{12} \ge \frac{3\tan\alpha - \cot\alpha}{12},$$

we obtain

$$\begin{aligned}
|\boldsymbol{v}_h|_{L^2(K)}^2 &= -\frac{2c_1c_2}{12}(\tan\alpha + \cot\alpha) + \frac{2c_1c_3}{12}(\cot\alpha - \tan\alpha) - \frac{2c_2c_3}{12}(\cot\alpha - \tan\alpha) \\
&\quad + c_1^2\left(\frac{1}{4}\tan\alpha + \frac{1}{12}\cot\alpha\right) + c_2^2\left(\frac{1}{12}\tan\alpha + \frac{1}{4}\cot\alpha\right) + c_3^2\left(\frac{1}{12}\tan\alpha + \frac{1}{12}\cot\alpha\right) \\
&= \frac{\tan\alpha + \cot\alpha}{12}(c_1 - c_2)^2 + \frac{\cot\alpha - \tan\alpha}{12}(c_1 + c_3)^2 + \frac{\cot\alpha - \tan\alpha}{12}(c_2 - c_3)^2 \\
&\quad + \frac{3\tan\alpha - \cot\alpha}{12}c_1^2 + \frac{\tan\alpha + \cot\alpha}{12}c_2^2 + \frac{3\tan\alpha - \cot\alpha}{12}c_3^2 \\
&\ge \frac{3\tan\alpha - \cot\alpha}{12}(c_1^2 + c_2^2 + c_3^2) \ge \frac{(3\tan\alpha - \cot\alpha)|K|}{36}|\nabla \times \boldsymbol{v}_h|_{L^2(K)}^2,
\end{aligned} \tag{5.13}$$

which leads to

$$|\nabla \times \boldsymbol{v}_h|_{L^2(K)}/|\boldsymbol{v}_h|_{L^2(K)} \le \sqrt{\frac{72}{3\sin^2\alpha - \cos^2\alpha}}h_{max}^{-1}.$$

Hence in this case, $c_{inv} = \sqrt{\frac{72}{3\sin^2\alpha - \cos^2\alpha}}$.

For a more general case, we could not obtain a nice inequality like (5.11) or (5.13), which leads to an accurate evaluation of c_{inv}.

5.2. Example 1: Test of convergence rate. Here we present an example to confirm the optimal convergence rate proved in Theorem 4.3. In this test, we choose the physical domain $\Omega = [0,1] \times [0,1]$, the time interval $I = [0,1]$, and the physical parameters $\epsilon_0 = \mu_0 = \omega_{pe} = \omega_{pm} = \Gamma_e = \Gamma_m = 1$ such that an exact solution for the 2D version of (2.1)–(2.4) is

$$\boldsymbol{E}(\boldsymbol{x},t) = \begin{pmatrix} \boldsymbol{E}_x \\ \boldsymbol{E}_y \end{pmatrix} = \frac{\sqrt{2}}{2}e^{-t}\cos t \begin{pmatrix} -\cos\pi x \sin\pi y \\ \sin\pi x \cos\pi y \end{pmatrix},$$

$$\boldsymbol{J}(\boldsymbol{x},t) = \begin{pmatrix} \boldsymbol{J}_x \\ \boldsymbol{J}_y \end{pmatrix} = \frac{\sqrt{2}}{2}e^{-t}\sin t \begin{pmatrix} -\cos\pi x \sin\pi y \\ \sin\pi x \cos\pi y \end{pmatrix},$$

TABLE 1
The errors obtained at $t = 1$ with full-mass matrix, and $\tau = 0.001$ on uniform rectangular meshes.

Meshes	$\|\|\boldsymbol{E} - \boldsymbol{E}_h\|\|_0$	Rates	$\|\|\nabla \times (\boldsymbol{E} - \boldsymbol{E}_h)\|\|_0$	Rates	$\|\|H - H_h\|\|_0$	Rates
5×5	0.012683610	—	0.112905069	—	0.112528790	—
10×10	0.006365158	0.9947	0.056519954	0.9982	0.056490585	0.9942
20×20	0.003185671	0.9986	0.028299764	0.9979	0.028270824	0.9987
40×40	0.001593184	0.9997	0.014155665	0.9994	0.014138525	0.9996
80×80	0.000796634	0.9999	0.007078579	0.9998	0.007069649	0.9999
160×160	0.000398322	0.9999	0.003539384	0.9999	0.003534873	0.9999

TABLE 2
The errors obtained at $t = 1$ with mass-lumping, and $\tau = 0.001$ on uniform rectangular meshes.

Meshes	$\|\|\boldsymbol{E} - \boldsymbol{E}_h\|\|_0$	Rates	$\|\|\nabla \times (\boldsymbol{E} - \boldsymbol{E}_h)\|\|_0$	Rates	$\|\|H - H_h\|\|_0$	Rates
5×5	0.092458183	—	0.599459477	—	0.190309198	—
10×10	0.025900523	1.8358	0.178949364	1.7441	0.097143198	0.9701
20×20	0.008092020	1.6784	0.061992600	1.5293	0.048875177	0.9910
40×40	0.003132964	1.3689	0.026301637	1.2369	0.024477120	0.9976
80×80	0.001428850	1.1326	0.012489717	1.0744	0.012243549	0.9994
160×160	0.000696130	1.0374	0.006159273	1.0199	0.006122400	0.9998

$$H(\boldsymbol{x}, t) = \sqrt{2}\pi e^{-t} \cos t \cos \pi x \cos \pi y,$$

$$K(\boldsymbol{x}, t) = \sqrt{2}\pi e^{-t} \sin t \cos \pi x \cos \pi y.$$

We solved this problem on a sequence of uniformly refined rectangular meshes using our leap-frog scheme (3.2)–(3.3) with a fixed time step $\tau = 0.001$. The obtained L^2 errors are presented in Table 1, which shows clearly an $O(h)$ convergence rate for $||\boldsymbol{E} - \boldsymbol{E}_h||_0$ and $||\boldsymbol{H} - \boldsymbol{H}_h||_0$. The observed convergence rate is consistent with our theoretical analysis.

Since we have to invert a mass matrix at each time step for the leap-frog scheme (3.2)–(3.3), in practical calculation we use a mass-lumping technique for the edge element. More specifically, we use the quadrature

$$\int_K \boldsymbol{\phi}_i \cdot \boldsymbol{\phi}_j dA = \frac{area(K)}{4} \sum_{n=1}^{4} (\boldsymbol{\phi}_i \cdot \boldsymbol{\phi}_j)(\boldsymbol{x}_n^K) \tag{5.14}$$

for any rectangular element K with vertices $\boldsymbol{x}_n^K, n = 1, 2, 3, 4$. Here $\boldsymbol{\phi}_i$ $(i = 1, 2, 3, 4)$ denote the edge element basis function of K. This quadrature has the nice feature that the mass matrix $(\boldsymbol{E}_h^{k+1}, \boldsymbol{\phi}_h)$ of (3.2) is diagonal [28, p. 352]. The obtained L^2 errors with mass-lumping technique are presented in Table 2. Though the errors in this case are about two times larger (as the mesh gets finer) than the full-mass matrix case, they still yield an $O(h)$ convergence rate for $||\boldsymbol{E} - \boldsymbol{E}_h||_0$ and $||\boldsymbol{H} - \boldsymbol{H}_h||_0$.

5.3. Demonstration of backward wave propagation phenomenon. Our goal of this section is to demonstrate the backward wave propagation phenomenon, which is one of the exotic properties for metamaterials. To simulate this phenomenon, we surround the computational domain by a perfectly matched layer (PML), which was originally introduced by Berenger in 1994 [7] to simulate the wave propagation in an unbounded domain. Since 1994, PML has been well studied (cf. [1, 4, 9, 39] and

references therein). For simplicity, here we use the classical 2D Berenger PML, whose governing equations can be written as

$$\varepsilon_0 \frac{\partial E_x}{\partial t} + \sigma_y E_x = \frac{\partial (H_{zx} + H_{zy})}{\partial y}, \tag{5.15}$$

$$\varepsilon_0 \frac{\partial E_y}{\partial t} + \sigma_x E_y = -\frac{\partial (H_{zx} + H_{zy})}{\partial x}, \tag{5.16}$$

$$\mu_0 \frac{\partial H_{zx}}{\partial t} + \sigma_{mx} H_{zx} = -\frac{\partial E_y}{\partial x}, \tag{5.17}$$

$$\mu_0 \frac{\partial H_{zy}}{\partial t} + \sigma_{my} H_{zy} = \frac{\partial E_x}{\partial y}, \tag{5.18}$$

where the parameters $\sigma_i, \sigma_{mi}, i = x, y$, are the electric and magnetic conductivities in the x- and y-directions, respectively. The functions $\sigma_{mi}, \sigma_i, i = x, y$, satisfy the impedance matching condition

$$\frac{\sigma_{mi}}{\mu_0} = \frac{\sigma_i}{\varepsilon_0}, \quad i = x, y,$$

so that the wave would be reflected at the interfaces between different material regions. Note that we can rewrite (5.15)–(5.16) in the vector form

$$\varepsilon_0 \frac{\partial \boldsymbol{E}}{\partial t} + \begin{pmatrix} \sigma_y & 0 \\ 0 & \sigma_x \end{pmatrix} \boldsymbol{E} = \nabla \times H_z, \tag{5.19}$$

where we used the 2D vector curl operator $\nabla \times H_z = \begin{pmatrix} \frac{\partial H}{\partial y} \\ -\frac{\partial H}{\partial x} \end{pmatrix}$ for $H_z = H_{zx} + H_{zy}$.

To couple the PML model with the scheme (3.2)–(3.3) in the metamaterial region, we construct a similar leap-frog scheme for solving the PML equations (5.19), (5.17)–(5.18) in the PML region: find $\boldsymbol{E}_h^{k+1} \in \boldsymbol{V}_h^0$, $H_{zx,h}^{k+\frac{3}{2}}, H_{zy,h}^{k+\frac{3}{2}} \in U_h$ such that

$$\varepsilon_0 \left(\frac{\boldsymbol{E}_h^{k+1} - \boldsymbol{E}_h^k}{\tau}, \boldsymbol{\phi}_h \right) + \left(\begin{pmatrix} \sigma_y & 0 \\ 0 & \sigma_x \end{pmatrix} \overline{\boldsymbol{E}}_h^{k+\frac{1}{2}}, \boldsymbol{\phi}_h \right) = \left(H_{zx,h}^{k+\frac{1}{2}} + H_{zy,h}^{k+\frac{1}{2}}, \nabla \times \boldsymbol{\phi}_h \right), \tag{5.20}$$

$$\mu_0 \left(\frac{\boldsymbol{H}_{zx,h}^{k+\frac{3}{2}} - \boldsymbol{H}_{zx,h}^{k+\frac{1}{2}}}{\tau}, \psi_{1,h} \right) + \left(\sigma_{mx} \overline{H}_{zx,h}^{k+1}, \psi_{1,h} \right) = -\left(\frac{\partial}{\partial x} E_{y,h}^{k+1}, \psi_{1,h} \right), \tag{5.21}$$

$$\mu_0 \left(\frac{\boldsymbol{H}_{zy,h}^{k+\frac{3}{2}} - \boldsymbol{H}_{zy,h}^{k+\frac{1}{2}}}{\tau}, \psi_{2,h} \right) + \left(\sigma_{my} \overline{H}_{zy,h}^{k+1}, \psi_{2,h} \right) = \left(\frac{\partial}{\partial y} E_{x,h}^{k+1}, \psi_{2,h} \right) \tag{5.22}$$

hold true for any $\boldsymbol{\phi}_h \in \boldsymbol{V}_h^0$ and any $\psi_{1,h}, \psi_{2,h} \in U_h$.

To simulate the backward wave propagation (see Examples 2 and 3 below), we use physical data similar to those introduced by Ziolkowski [47]. We choose a uniform mesh size $h = 0.0001$ m. By applying the C_{inv} derived in (5.6) and $C_v = 3 \cdot 10^8$ m/s to the CFL condition (4.2), we have $\tau \le \frac{h}{C_{inv} C_v} = \frac{10}{3\sqrt{6}} \cdot 10^{-13} \approx 1.36 \cdot 10^{-13}$. Hence in our numerical test, we just use $\tau = 10^{-13}$. Moreover, we choose the center

frequency of the refraction index is $f_0 = 30$ GHz, which corresponds to the free-space wavelength $\lambda_0 = 0.01$ m, and the physical parameters

$$\Gamma_e = \Gamma_m = \Gamma = 10^8 s^{-1}, \quad \omega_{pe} = \omega_{pm} = \omega_p = \sqrt{2}\omega_0 \equiv 2\pi\sqrt{2} f_0,$$

which correspond to the refraction index at the center frequency,

$$n(\omega_0) = \sqrt{\frac{\epsilon(\omega_0)\mu(\omega_0)}{\epsilon_0\mu_0}} = 1 - \frac{\omega_p^2}{\omega_0(\omega_0 - i\Gamma)} \approx -1,$$

where the vacuum permeability μ_0 and the vacuum permittivity ϵ_0 are

$$\mu_0 = 4\pi \times 10^{-7} \text{ newtons/ampere}^2, \quad \epsilon_0 = 8.8541878176 \times 10^{-12} \text{ force/meter}.$$

Example 2. In this example, the physical domain is chosen to be $[0, 0.07]$ m $\times$ $[0, 0.064]$ m. The incident source wave (imposed as the E_y component) varies in space as $e^{-(x-0.03)^2/(50h)^2}$ and in time as [47]

$$f(t) = \begin{cases} 0 & \text{for } t < 0, \\ g_1(t)\sin(\omega_0 t) & \text{for } 0 < t < mT_p, \\ \sin(\omega_0 t) & \text{for } mT_p < t < (m+k)T_p, \\ g_2(t)\sin(\omega_0 t) & \text{for } (m+k)T_p < t < (2m+k)T_p, \\ 0 & \text{for } t > (2m+k)T_p, \end{cases}$$

where we denote $T_p = 1/f_0$, and

$$g_1(t) = 10x_1^3 - 15x_1^4 + 6x_1^5, \quad x_1 = t/mT_p,$$

$$g_2(t) = 1 - (10x_2^3 - 15x_2^4 + 6x_2^5), \quad x_2 = (t - (m+k)T_p)/mT_p.$$

In our simulation, we use $m = 2, k = 100$, and a PML with 12 cells in thickness around the physical domain.

The beam source is located at $x = 0.004$ m, the metamaterial slab is from 0.024 m to 0.044 m in the x-direction, and from 0.002 m to 0.062 m in the y-direction. Outside the slab is a vacuum. We solved this example using 480736 rectangular elements, which lead to the total DOFs (degrees of freedom) for H_z to be 480736, and the total DOFs for $\boldsymbol{E}$ to be 960084. The obtained E_y components at various time steps are plotted in Figure 1. From Figure 1, we can see that before the wave enters into the metamaterial region (bounded by the box), the wave propagates as usual. Once the wave enters into the metamaterial, the wave reverses its propagation direction due to the negative refraction index of the metamaterial. As the wave reaches the other end of the metamaterial slab, we see the refocusing property of metamaterials, i.e., the original wave source refocuses at the other side of the slab. After the wave exits the slab, the wave propagates in free space as usual again. We like to remark that a coarse mesh up to $h = \frac{1}{10}\lambda_0 = 0.001$ m can still catch the backward wave propagation phenomenon (see Figure 2). The only problem is that the wave resolution is not that good.

Example 3. Note that our theoretical results hold true for triangular elements too. To demonstrate this, we use a triangular metamaterial slab to demonstrate the

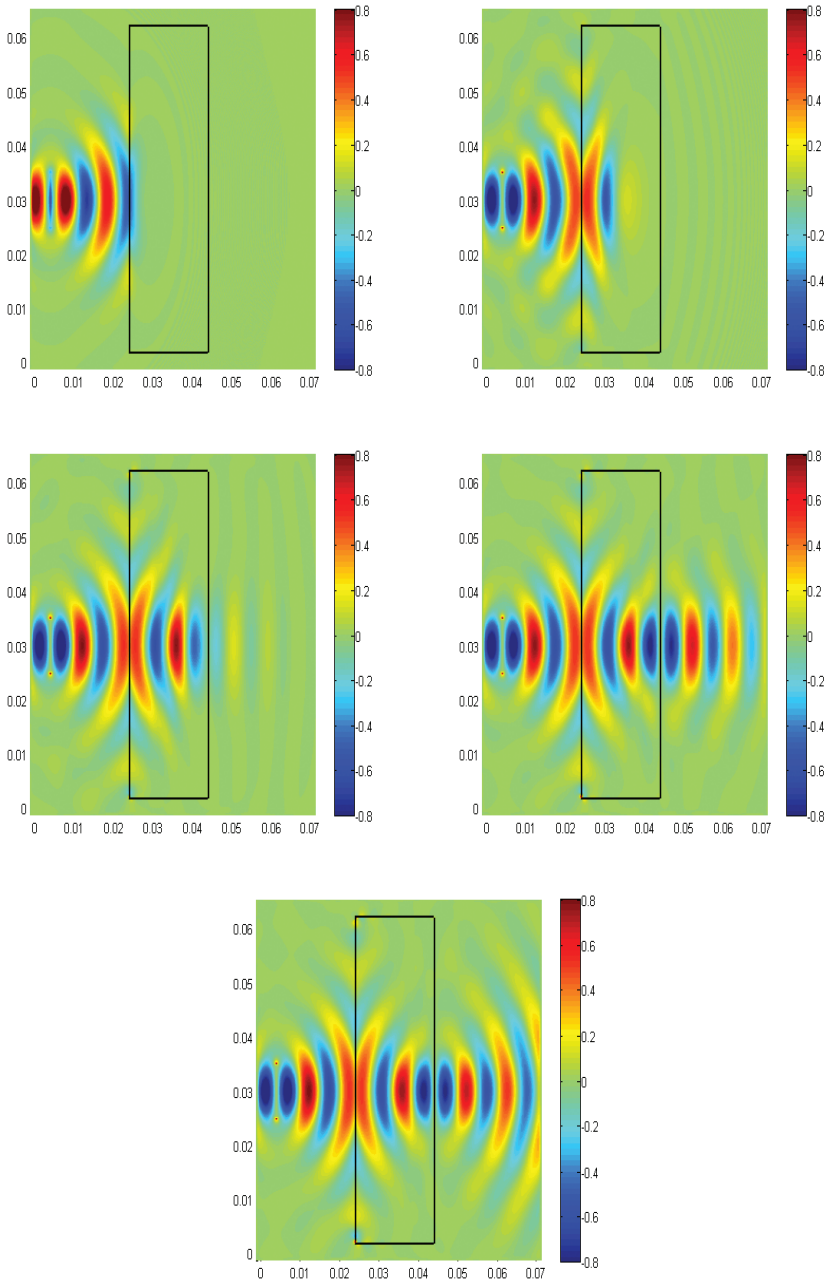

FIG. 1. *Example* 2. *Electric fields* E_y *solved with* $h = \frac{1}{100}\lambda_0$ *at various time steps. Top left:* 1200 *steps. Top right:* 2000 *steps. Middle left:* 3000 *steps. Middle right:* 4000 *steps. Bottom:* 5000 *steps.*

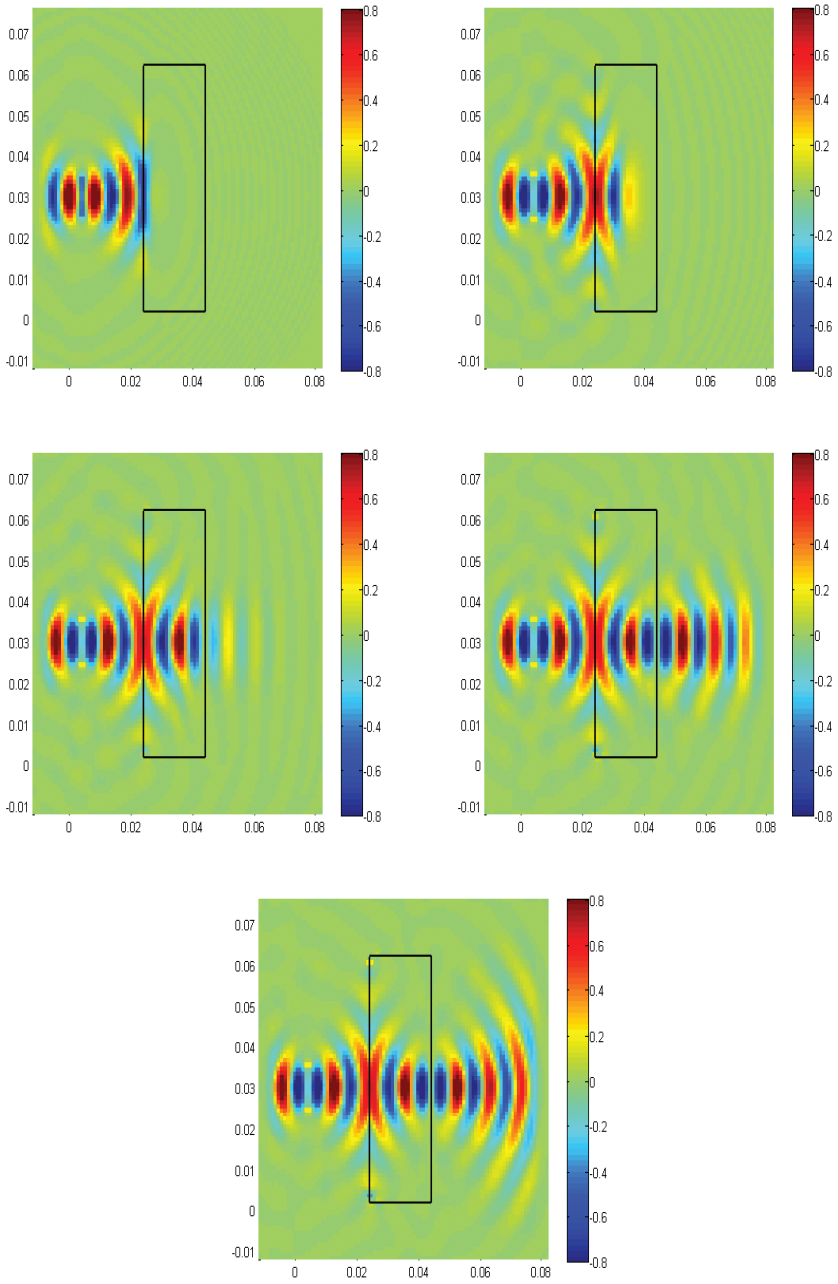

FIG. 2. *Example* 2. *Electric fields* E_y *solved with* $h = \frac{1}{10}\lambda_0$ *at various time steps. Top left:* 1200 *steps. Top right:* 2000 *steps. Middle left:* 3000 *steps. Middle right:* 4000 *steps. Bottom:* 5000 *steps.*

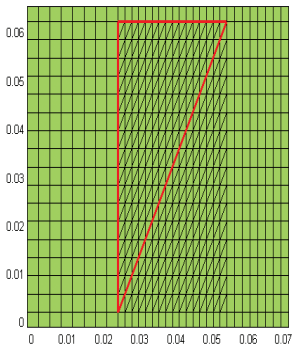

FIG. 3. *An exemplary mixed mesh used for the triangular metamaterial slab.*

backward wave propagation phenomenon and Snell's law. The physical domain is chosen to be $[0, 0.07]$ m $\times$ $[0, 0.064]$ m. The incident source wave is still located at $x = 0.004$ m, but it is imposed as the H_z component. We choose a triangular metamaterial slab, whose boundary is determined by points $(0.024, 0.02)$, $(0.024, 0.062)$, and $(0.054, 0.062)$. Outside this slab is a vacuum. In this case, a triangular mesh is used for the metamaterial slab and its neighboring elements. To accommodate the PML easily and accurately, we use a rectangular mesh in the vacuum region and PML region, which make this test problem more challenging. On the rectangular elements, we still use the lowest-order edge elements.

An exemplary mesh is shown in Figure 3, which is quite coarse for illustration purposes. The results presented below used a mesh by uniformly refining the one given in Figure 3; i.e., the real mesh has 524288 and 327680 triangular elements and rectangular elements, respectively. Hence the total number of DOFs for $\boldsymbol{E}$ is 1440192. In this case, the time step $\tau = 5 \cdot 10^{-14}$. The calculated E_y components at various time steps are plotted in Figure 4, which shows clearly that the wave propagates backward inside the metamaterial slab. After the wave exits the metamaterial region, the wave bends its propagation direction according to Snell's law.

5.4. Investigation of another PML. In this last section, we show some results obtained by using an unsplit PML. The original split PML proposed by Berenger [7] was found to be only weakly well posed, and it may suffer explosive instability [1, 39]. Later, Becache and Joly [4] showed that the split PML has at most a linearly growing solution in the late time. Hence, it is suggested that an unsplit PML may be the most appropriate for problems requiring long-time simulation [5].

Following the idea of [39], we can convert the split PML (5.15)–(5.18) into an unsplit PML. Let us define the Fourier transform of a function $f(t)$ as $\hat{f}(\omega) = \int_{-\infty}^{\infty} e^{i\omega t} f(t) dt$.

Taking the Fourier transform of (5.17) and (5.18), we have

$$(i\omega\mu_0 + \sigma_{mx})\hat{H}_{zx} + \frac{\partial \hat{E}_y}{\partial x} = 0,$$

$$(i\omega\mu_0 + \sigma_{my})\hat{H}_{zy} - \frac{\partial \hat{E}_x}{\partial y} = 0.$$

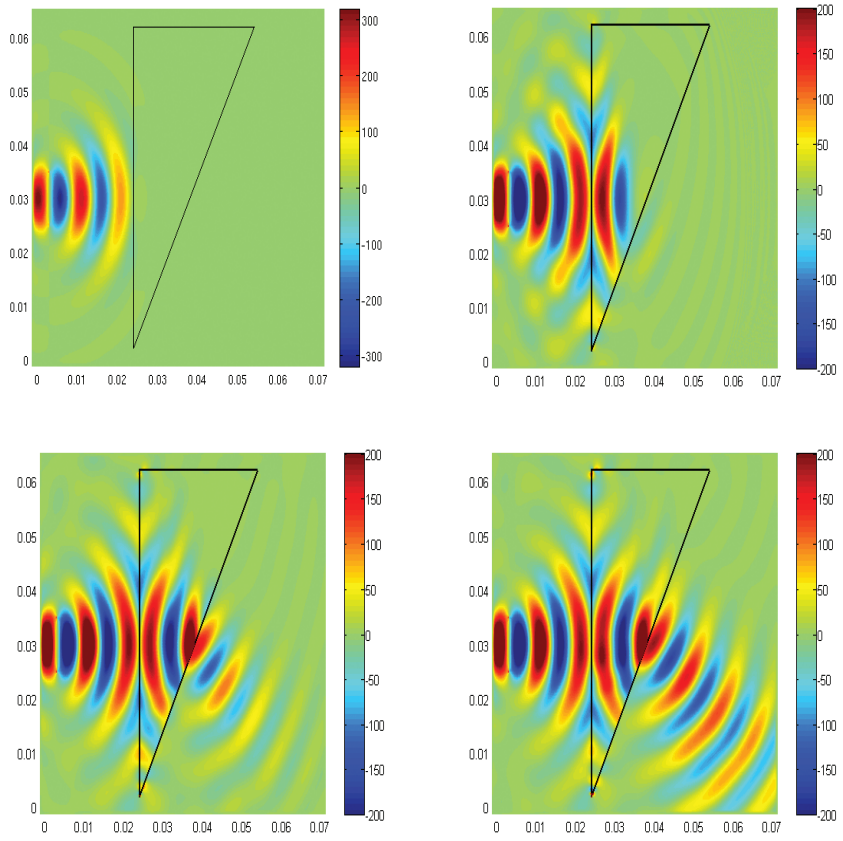

FIG. 4. *Example* 3. *Electric fields* E_y *at various time steps. Top left:* 2000 *steps. Top right:* 4000 *steps. Bottom left:* 6000 *steps. Bottom right:* 8000 *steps.*

Multiplying the first and second equations by $(i\omega\mu_0+\sigma_{my})$ and $(i\omega\mu_0+\sigma_{mx})$, respectively, then adding the results together and using the definition $H_z = H_{zx} + H_{zy}$, we obtain

(5.23)
$$(i\omega\mu_0+\sigma_{mx})(i\omega\mu_0+\sigma_{my})\hat{H}_z + i\omega\mu_0\left(1+\frac{\sigma_{my}}{i\omega\mu_0}\right)\frac{\partial\hat{E}_y}{\partial x} - i\omega\mu_0\left(1+\frac{\sigma_{mx}}{i\omega\mu_0}\right)\frac{\partial\hat{E}_x}{\partial y} = 0.$$

Introducing auxiliary variables

(5.24)
$$\hat{P}_x = \frac{1}{i\omega\mu_0}\hat{E}_x, \quad \hat{P}_y = \frac{1}{i\omega\mu_0}\hat{E}_y, \quad \hat{Q}_z = \frac{1}{i\omega\mu_0}\hat{H}_z,$$

and we can rewrite (5.23) as follows:

(5.25)
$$[i\omega\mu_0+(\sigma_{mx}+\sigma_{my})]\hat{H}_z+\sigma_{mx}\sigma_{my}\hat{Q}_z+\frac{\partial(\hat{E}_y+\sigma_{my}\hat{P}_y)}{\partial x}-\frac{\partial(\hat{E}_x+\sigma_{mx}\hat{P}_x)}{\partial y} = 0.$$

Changing (5.24) and (5.25) into time domain, and putting the original PML

equation (5.19) together, we obtain the unsplit PML model equations:

$$\varepsilon_0 \frac{\partial \boldsymbol{E}}{\partial t} + \begin{pmatrix} \sigma_y & 0 \\ 0 & \sigma_x \end{pmatrix} \boldsymbol{E} = \nabla \times H_z, \tag{5.26}$$

$$\mu_0 \frac{\partial H_z}{\partial t} + (\sigma_{mx} + \sigma_{my}) H_z + \nabla \times \boldsymbol{E} + \sigma_{mx}\sigma_{my} Q_z + \sigma_{my} \frac{\partial P_y}{\partial x} - \sigma_{mx} \frac{\partial P_x}{\partial y} = 0, \tag{5.27}$$

$$\mu_0 \frac{\partial P_x}{\partial t} = E_x, \tag{5.28}$$

$$\mu_0 \frac{\partial P_y}{\partial t} = E_y, \tag{5.29}$$

$$\mu_0 \frac{\partial Q_z}{\partial t} = H_z. \tag{5.30}$$

To couple with our metamaterial model, we construct a leap-frog scheme for solving the unsplit PML equations: find $\boldsymbol{E}_h^{k+1} \in \boldsymbol{V}_h^0, H_{z,h}^{k+\frac{3}{2}} \in U_h$ such that

$$\varepsilon_0 \left(\frac{\boldsymbol{E}_h^{k+1} - \boldsymbol{E}_h^k}{\tau}, \boldsymbol{\phi}_h \right) + \left(\begin{pmatrix} \sigma_y & 0 \\ 0 & \sigma_x \end{pmatrix} \overline{\boldsymbol{E}}_h^{k+\frac{1}{2}}, \boldsymbol{\phi}_h \right) = \left(H_{z,h}^{k+\frac{1}{2}}, \nabla \times \boldsymbol{\phi}_h \right), \tag{5.31}$$

$$\mu_0 \frac{P_{x,h}^{k+\frac{3}{2}} - P_{x,h}^{k+\frac{1}{2}}}{\tau} = E_{x,h}^{k+1}, \tag{5.32}$$

$$\mu_0 \frac{P_{y,h}^{k+\frac{3}{2}} - P_{y,h}^{k+\frac{1}{2}}}{\tau} = E_{y,h}^{k+1}, \tag{5.33}$$

$$\mu_0 \frac{Q_{z,h}^{k+1} - Q_{z,h}^{k}}{\tau} = H_{z,h}^{k+\frac{1}{2}}, \tag{5.34}$$

$$\begin{aligned} &\mu_0 \left(\frac{H_{z,h}^{k+\frac{3}{2}} - H_{z,h}^{k+\frac{1}{2}}}{\tau}, \psi_h \right) + \left((\sigma_{mx} + \sigma_{my}) \overline{H}_{z,h}^{k+1}, \psi_h \right) + \left(\nabla \times \boldsymbol{E}_h^{k+1}, \psi_h \right) \\ &\quad + \left(\sigma_{mx}\sigma_{my} Q_{z,h}^{k+1}, \psi_h \right) + \left(\sigma_{my} \frac{\partial \overline{P}_{y,h}^{k+1}}{\partial x} - \sigma_{mx} \frac{\partial \overline{P}_{x,h}^{k+1}}{\partial y}, \psi_h \right) = 0 \end{aligned} \tag{5.35}$$

hold true for any $\boldsymbol{\phi}_h \in \boldsymbol{V}_h^0$ and any $\psi_h \in U_h$.

Example 4. We simulate Example 2 by using the same data, except that we replaced the split PML by this unsplit PML scheme. We obtain very similar results; see Figure 5, which basically has no difference from Figure 1. The reason may be that our simulation is not long enough to see the real advantage of the unsplit PML.

Example 5. This final example is another demonstration of the unsplit PML. In this example, the physical domain is chosen to be $[0, 0.13]$ m $\times$ $[0, 0.08]$ m. The incident wave is a point source wave (the same $f(t)$ in Example 2) located at the point (0.02 m, 0.04 m), which varies only in time and has the same form as Example 2. Here the wave is imposed as the H_z component, and the metamaterial slab is from 0.04 m to 0.08 m in the x-direction, and from 0.002 m to 0.078 m in the y-direction. Outside the slab is a vacuum. This example is solved using 285776 uniform rectangular elements with a mesh size $h = 0.0002$, which lead to the total DOFs for H_z to be 285776, and the total DOFs for E to be 570454. The calculated H_z and E_y components at various time steps with a time step size $\tau = 2 \cdot 10^{-13}$ are plotted in Figures 6 and 7, respectively. These figures show the effectiveness of the unsplit PML, and demonstrate the nice refocusing property for metamaterials.

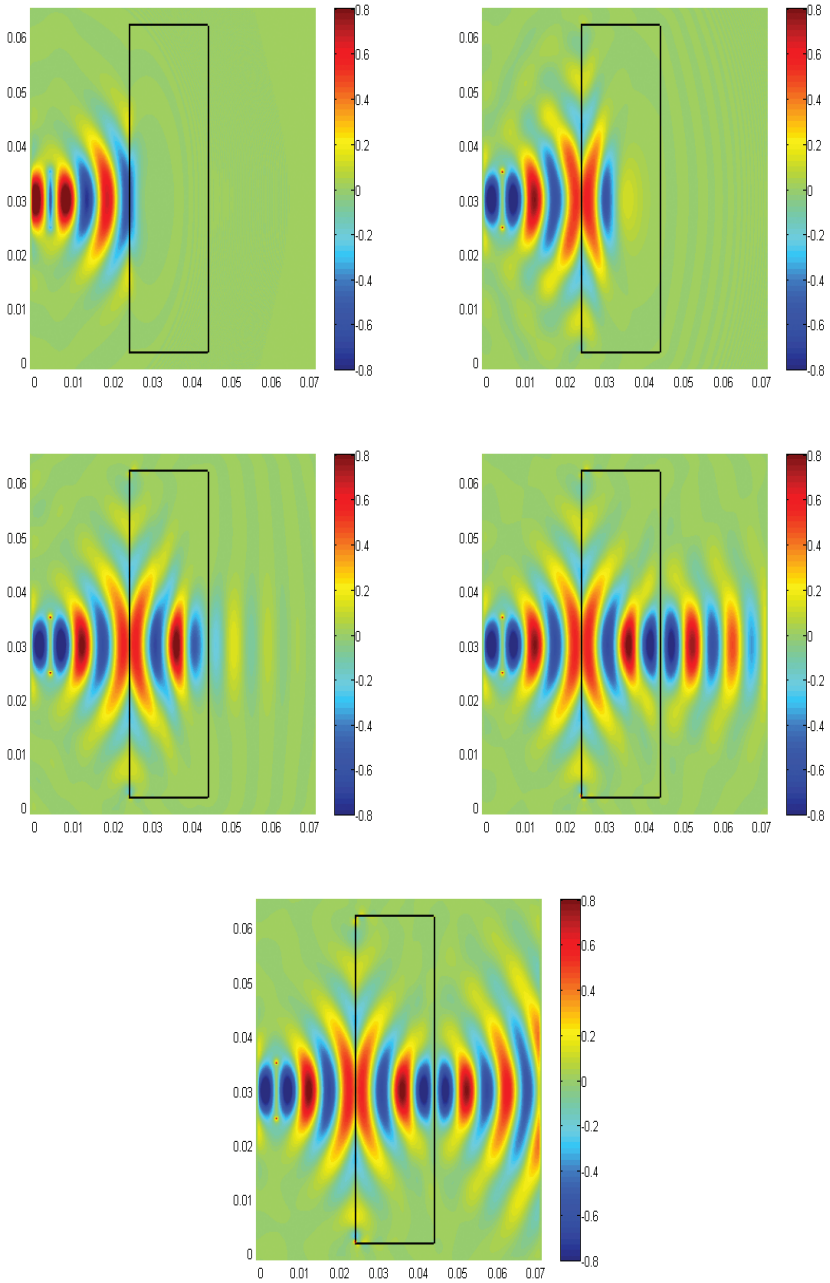

FIG. 5. *Electric fields E_y at various time steps used the unsplit PML. Top left:* 1200 *steps. Top right:* 2000 *steps. Middle left:* 3000 *steps. Middle right:* 4000 *steps. Bottom:* 5000 *steps.*

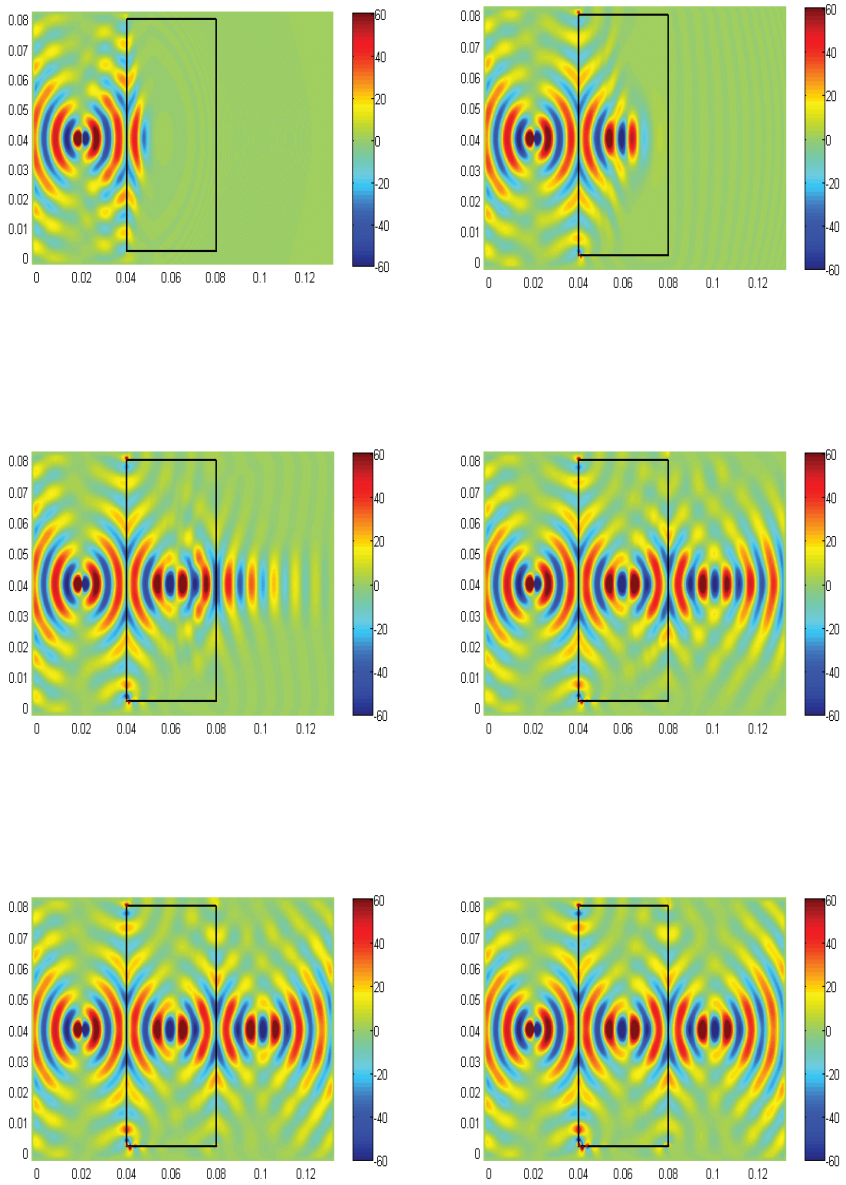

FIG. 6. *Example* 5. *Electric fields* E_y *at various time steps used the unsplit PML. Top left:* 1000 *steps. Top right:* 2000 *steps. Middle left:* 3000 *steps. Middle right:* 4000 *steps. Bottom left:* 5000 *steps. Bottom right:* 6000 *steps.*

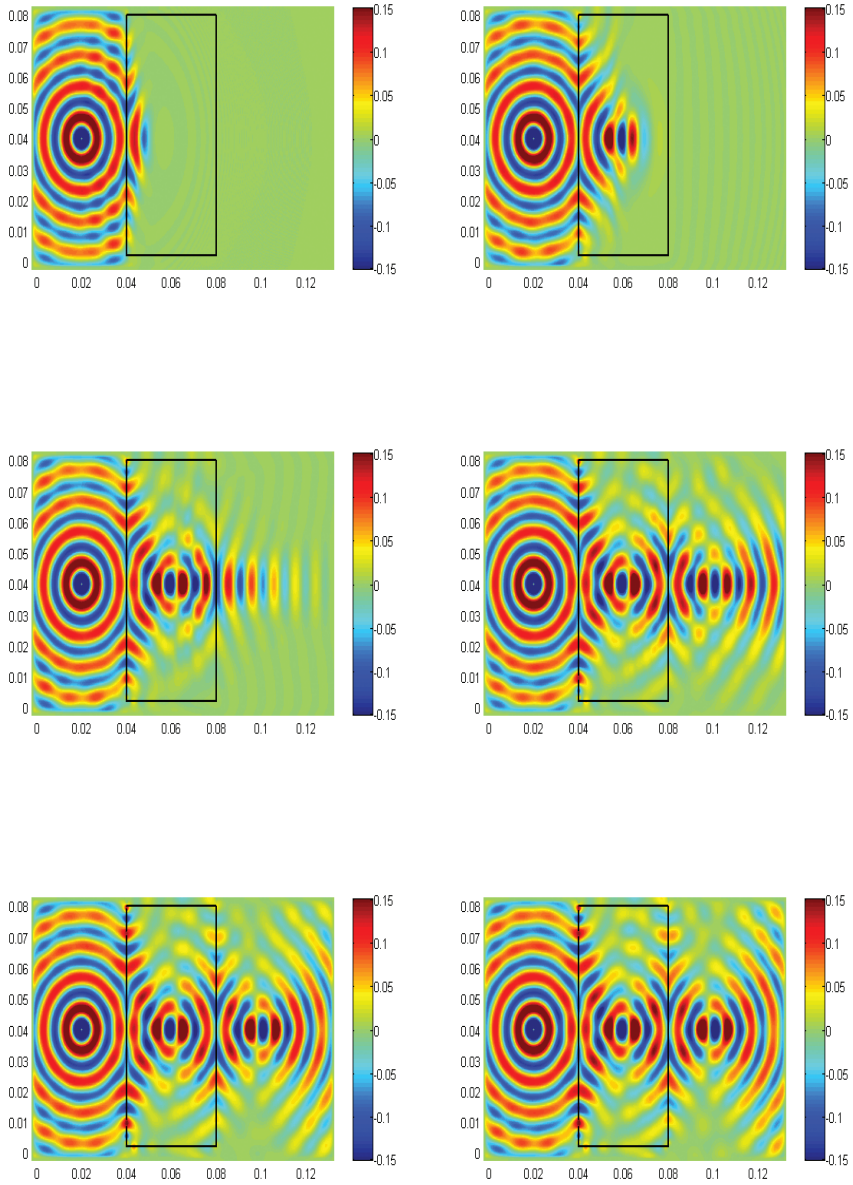

FIG. 7. *Example* 5. *Magnetic fields* H_z *at various time steps used the unsplit PML. Top left:* 1000 *steps. Top right:* 2000 *steps. Middle left:* 3000 *steps. Middle right:* 4000 *steps. Bottom left:* 5000 *steps. Bottom right:* 6000 *steps.*

6. Conclusions. In conclusion, we have developed a leap-frog-type finite element method for modeling the backward wave propagation in metamaterials. The stability and error estimate of the proposed method are investigated. The algorithm is first tested for the optimal convergence rate using a smooth analytic solution, then generalized to the coupled metamaterial and vacuum media case. The simulation results not only confirm the theoretical analysis, but also demonstrate the effectiveness of our algorithm for modeling various wave propagation phenomena occurring in heterogeneous media. More efficient numerical techniques such as multiscale techniques [44], discontinuous Galerkin methods [15, 18, 20, 21, 23], and adaptive finite element methods [2, 12, 37] will be investigated in the future.

Acknowledgment. The authors are very grateful to the two referees for their insightful comments which improved our paper.

REFERENCES

[1] S. Abarbanel, D. Gottlieb, and J.S. Hesthaven, *Long time behavior of the perfectly matched layer equations in computational electromagnetics*, J. Sci. Comput., 17 (2002), pp. 405–421.

[2] M. Ainsworth and J. Coyle, *Hierarchic hp-edge element families for Maxwell's equations on hybrid quadrilateral/triangular meshes*, Comput. Methods Appl. Mech. Engrg., 190 (2001), pp. 6709–6733.

[3] H.T. Banks, V.A. Bokil, and N.L. Gibson, *Analysis of stability and dispersion in a finite element method for Debye and Lorentz media*, Numer. Methods Partial Differential Equations, 25 (2009), pp. 885–917.

[4] E. Becache and P. Joly, *On the analysis of Berenger's perfectly matched layers for Maxwell's equations*, Math. Model. Numer. Anal., 36 (2002), pp. 87–119.

[5] E. Becache, P.G. Petropoulos, and S.D. Gedney, *On the long-time behavior of unsplit perfectly matched layers*, IEEE Trans. Antennas and Propagation, 52 (2004), pp. 1335–1342.

[6] A.S. Bonnet-Ben Dhia, P. Ciarlet Jr., and C.M. Zwölf, *Two- and three-field formulations for wave transmission between media with opposite sign dielectric constants*, J. Comput. Appl. Math., 204 (2007), pp. 408–417.

[7] J.P. Berenger, *A perfectly matched layer for the absorption of electromagnetic waves*, J. Comput. Phys., 114 (1994), pp. 185–200.

[8] Z. Chen, Q. Du, and J. Zou, *Finite element methods with matching and nonmatching meshes for Maxwell equations with discontinuous coefficients*, SIAM J. Numer. Anal., 37 (2000), pp. 1542–1570.

[9] F. Collino and P. Monk, *The perfectly matched layer in curvilinear coordinates*, SIAM J. Sci. Comput., 19 (1998), pp. 2061–2090.

[10] B. Cockburn, F. Li, and C.-W. Shu, *Locally divergence-free discontinuous Galerkin methods for the Maxwell equations*, J. Comput. Phys., 194 (2004), pp. 588–610.

[11] T.J. Cui, D.R. Smith, and R. Liu, eds., *Metamaterials: Theory, Design, and Applications*, Springer, New York, 2009.

[12] L. Demkowicz, J. Kurtz, D. Pardo, M. Paszynski, W. Rachowicz, and A. Zdunek, *Computing with hp-Adaptive Finite Elements. Vol.* 2. *Frontiers: Three Dimensional Elliptic and Maxwell Problems with Applications*, CRC Press, Taylor and Francis, Boca Raton, FL, 2006.

[13] N. Engheta and R.W. Ziolkowski, *Electromagnetic Metamaterials: Physics and Engineering Explorations*, Wiley-IEEE Press, Hoboken, NJ, 2006.

[14] P. Fernandes and M. Raffetto, *Well posedness and finite element approximability of time-harmonic electromagnetic boundary value problems involving bianisotropic materials and metamaterials*, Math. Models Methods Appl. Sci., 19 (2009), pp. 2299–2335.

[15] L. Fezoui, S. Lanteri, S. Lohrengel, and S. Piperno, *Convergence and stability of a discontinuous Galerkin time-domain methods for the* 3*D heterogeneous Maxwell equations on unstructured meshes*, Model. Math. Anal. Numer., 39 (2005), pp. 1149–1176.

[16] Y. Hao and R. Mittra, *FDTD Modeling of Metamaterials: Theory and Applications*, Artech House, Norwood, MA, 2008.

[17] I. Harari and T.J.R. Hughes, *What are C and h?: Inequalities for the analysis and design of finite element methods*, Comput. Methods Appl. Mech. Engrg., 97 (1992), pp. 157–192.
[18] J.S. Hesthaven and T. Warburton, *Nodal Discontinuous Galerkin Methods: Algorithms, Analysis, and Applications*, Springer, New York, 2008.
[19] R. Hiptmair, *Finite elements in computational electromagnetism*, Acta Numer., 11 (2002), pp. 237–339.
[20] P. Houston, I. Perugia, A. Schneebeli, and D. Schötzau, *Interior penalty method for the indefinite time-harmonic Maxwell equations*, Numer. Math., 100 (2005), pp. 485–518.
[21] Y. Huang, J. Li, and W. Yang, *Interior penalty DG methods for Maxwell's equations in dispersive media*, J. Comput. Phys., 230 (2011), pp. 4559–4570.
[22] Y. Huang, J. Li, W. Yang, and S. Sun, *Superconvergence of mixed finite element approximations to 3-D Maxwell's equations in metamaterials*, J. Comput. Phys., 230 (2011), pp. 8275–8289.
[23] J. Li, *Posteriori error estimation for an interior penalty discontinuous Galerkin method for Maxwell's equations in cold plasma*, Adv. Appl. Math. Mech., 1 (2009), pp. 107–124.
[24] J. Li, *Numerical convergence and physical fidelity analysis for Maxwell's equations in metamaterials*, Comput. Methods Appl. Mech. Engrg., 198 (2009), pp. 3161–3172.
[25] J. Li and A. Wood, *Finite element analysis for wave propagation in double negative metamaterials*, J. Sci. Comput., 32 (2007), pp. 263–286.
[26] T. Lu, P. Zhang, and W. Cai, *Discontinuous Galerkin methods for dispersive and lossy Maxwell's equations and PML boundary conditions*, J. Comput. Phys., 200 (2004), pp. 549–580.
[27] P. Markos and C.M. Soukoulis, *Wave Propagation: From Electrons to Photonic Crystals and Left-Handed Materials*, Princeton University Press, Princeton, NJ, 2008.
[28] P. Monk, *Finite Element Methods for Maxwell's Equations*, Oxford University Press, New York, 2003.
[29] J.-C. Nédélec, *Mixed finite elements in R^3*, Numer. Math., 35 (1980), pp. 315–341.
[30] Z. Qiao, C. Yao, and S. Jia, *Superconvergence and extrapolation analysis of a nonconforming mixed finite element approximation for time-harmonic Maxwell's equations*, J. Sci. Comput., 46 (2011), pp. 1–19.
[31] R.N. Rieben, G.H. Rodrigue, and D.A. White, *A high order mixed vector finite element method for solving the time dependent Maxwell equations on unstructured grids*, J. Comput. Phys., 204 (2005), pp. 490–519.
[32] C. Scheid and S. Lanteri, *Convergence of a Discontinuous Galerkin Scheme for the Mixed Time Domain Maxwell's Equations in Dispersive Media*, Tech. report INRIA-00597374, INRIA Sophia Antipolis, 2011. Downloadable from http://hal.inria.fr/docs/00/59/73/74/PDF/RR-7634.pdf.
[33] Ch. Schwab, *p- and hp-Finite Element Methods*, Oxford University Press, New York, 1998.
[34] S. Shaw, *Finite element approximation of Maxwell's equations with Debye memory*, Adv. Numer. Anal., 2010 (2010), 923832.
[35] A. Shelby, D.R. Smith, and S. Schultz, *Experimental verification of a negative index of refraction*, Science, 292 (2001), pp. 489–491.
[36] D.R. Smith, W.J. Padilla, D.C. Vier, S.C. Nemat-Nasser, and S. Schultz, *Composite medium with simultaneously negative permeability and permittivity*, Phys. Rev. Lett., 84 (2000), pp. 4184–4187.
[37] P. Solin, L. Dubcova, J. Cerveny, and I. Dolezel, *Adaptive hp-FEM with arbitrary-level hanging nodes for Maxwell's equations*, Adv. Appl. Math. Mech., 2 (2010), pp. 518–532.
[38] A. Taflove and S.C. Hagness, *Computational Electrodynamics: The Finite-Difference Time-Domain Method*, 3rd ed., Artech House, Boston, MA, 2005.
[39] E. Turkel and A. Yefet, *Absorbing PML boundary layers for wave-like equations*, Appl. Numer. Math., 27 (1998), pp. 533–557.
[40] V. Veselago, *Electrodynamics of substances with simultaneously negative values of sigma and mu*, Sov. Phys. Usp., 10 (1968), pp. 509–514.
[41] V. Veselago, L. Braginsky, V. Shklover, and C. Hafner, *Negative refractive index materials*, J. Comput. Theoret. Nanosci., 3 (2006), pp. 1–30.
[42] B. Wang, Z. Xie, and Z. Zhang, *Error analysis of a discontinuous Galerkin method for Maxwell equations in dispersive media*, J. Comput. Phys., 229 (2010), pp. 8552–8563.
[43] T. Warburton and J.S. Hesthaven, *On the constants in hp-finite element trace inverse inequalities*, Comput. Methods Appl. Mech. Engrg., 192 (2003), pp. 2765–2773.
[44] Y. Zhang, L.-Q. Cao, and Y.-S. Wong, *Multiscale computations for 3D time-dependent Maxwell's equations in composite materials*, SIAM J. Sci. Comput., 32 (2010), pp. 2560–2583.

[45] S. Zhao, *High-order FDTD methods for transverse electromagnetic systems in dispersive inhomogeneous media*, Opt. Lett., 36 (2011), pp. 3245–3247.
[46] W.Y. Zheng, Z. Chen, and L. Wang, *An adaptive finite element method for the H-ψ formulation of time-dependent eddy current problems*, Numer. Math., 103 (2006), pp. 667–689.
[47] R.W. Ziolkowski, *Pulsed and CW Gaussian beam interactions with double negative metamaterial slabs*, Opt. Express, 11 (2003), pp. 662–681.